

A novel non-convex minimax p -th order concave penalty function approach to low-rank tensor completion

Hongbing Zhang*, Bing Zheng

School of Mathematics and Statistics, Lanzhou University, Lanzhou 730000, P.R. China

Abstract

The low-rank tensor completion (LRTC) problem aims to reconstruct a tensor from partial sample information, which has attracted significant interest in a wide range of practical applications such as image processing and computer vision. Among the various techniques employed for the LRTC problem, non-convex relaxation methods have been widely studied for their effectiveness in handling tensor singular values, which are crucial for accurate tensor recovery. While the minimax concave penalty (MCP) non-convex relaxation method has achieved promising results in tackling the LRTC problem and gained widely adopted, it exhibits a notable limitation: insufficient penalty on small singular values during the singular value handling process, resulting in inefficient tensor recovery. To address this issue and enhance recovery performance, a novel minimax p -th order concave penalty (MPCP) function is proposed. Based on this novel function, a tensor p -th order τ norm is proposed as a non-convex relaxation for tensor rank approximation, thereby establishing an MPCP-based LRTC model. Furthermore, theoretical convergence guarantees are rigorously established for the proposed method. Extensive numerical experiments conducted on multiple real datasets demonstrate that the proposed method outperforms the state-of-the-art methods in both visual quality and quantitative metrics.

Keywords: Low-rank tensor completion, tensor nuclear norm, non-convex relaxation, minimax concave penalty function, convergence analysis.

1 Introduction

Tensors, as higher-order generalizations of vectors and matrices, are widely acknowledged to capture intrinsic structural information in multimodal/multi-relational data more effectively. The processing of tensor data has been increasingly recognized as a pivotal component across diverse domains, such as image/video processing, magnetic resonance imaging data recovery [26], machine learning[10, 29], computer vision[15, 32], and pattern recognition[7, 35]. Nevertheless, in practical application scenarios, real-world tensor data are frequently corrupted due to unpredictable or unavoidable disturbances, thereby driving the demand for tensor completion techniques to restore multidimensional data integrity.

*Corresponding author. E-mail: zhb123abc@163.com.

It is well-established that tensor rank minimization has been widely adopted as a prevalent approach for addressing low-rank tensor completion (LRTC) problem. However, the definition of tensor rank is not unique. The mainstream definitions of tensor rank are CANDECOMP/PARAFAC (CP) rank based on CP decomposition [5], Tucker rank based on Tucker decomposition [25], and tubal rank [11] induced by tensor singular value decomposition (t-SVD) [12]. Nevertheless, directly solving the CP rank is NP-hard [6]. The tubal rank can better maintain the data structure compared with CP rank and Tucker rank. Subsequently, Zhang et al. [33] defined the tensor nuclear norm (TNN) based on tensor tubal rank to solve the LRTC problem and obtained the advanced tensor recovery results. Recently, Zheng et al. [39] proposed a new form of rank (N-tubal rank) based on tubal rank, which adopts a new unfold method of higher-order tensors into third-order tensors in various directions. This method enables t-SVD to be applied to higher-order tensor.

Although the TNN method has become a commonly used method for solving the LRTC problem, it applies the same penalty to all singular values, which will leads to suboptimal solutions. In contrast, non-convex relaxation methods have garnered widespread attention due to their ability to handle tensor singular values more effectively. To achieve non-convex relaxation, various functions and methods have been employed by researchers, including the logarithmic function [4], the minimax concave penalty (MCP) function [38, 22], and the t-Schatten- p norm [13]. These methods, with their distinct non-convex penalty mechanisms, offer greater flexibility in handling tensor singular values, leading to improved performance in tensor recovery problem.

Recently, the MCP function as a non-convex relaxation has achieved promising results in the LRTC problem [2, 22, 23, 30, 36]. In [22], the MCP function with different parameters were employed to penalize different singular values, enhancing overall effectiveness. However, as the problem scale increases, parameter selection for each singular value becomes extremely challenging. The bivariate equivalent MCP method proposed in [36] enables parameters to be updated iteratively, significantly improving recovery performance. [2] proposed a truncated MCP method to penalize singular values, achieving enhanced results by adjusting truncated rate and corresponding MCP function parameters. Essentially, these methods still rely on various parameter adjustment strategies of the MCP function to obtain good recovery results. Nevertheless, the inherent limitation of the MCP function, inadequate penalization of small singular values, remains unresolved by the above methods. To address this issue, a novel minimax p -th order concave penalty (MPCP) function is proposed. The proposed MPCP function not only preserves the MCP function's property of protecting large singular values but also imposes stronger penalties on small singular values. Specifically, the main contributions of this paper are summarized as follows.

First, a novel MPCP function is proposed to address the deficiency of the MCP function in insufficient penalization of small singular values. Key properties of the MPCP function are systematically analyzed and mathematically proven. To enable efficient optimization for LRTC applications, the proximal operator for the MPCP function is derived. Furthermore, tensor extensions of the MPCP function, including tensor p -th order τ norm definition and associated mathematical properties, are thoroughly investigated.

Second, a new MPCP-based LRTC model is developed, accompanied by a solving algo-

rithm implemented through the alternating direction multipliers method (ADMM). Rigorous theoretical analysis of the algorithm's convergence is provided to guarantee the proposed method numerical stability.

Third, comprehensive experiments are conducted on multi-dimensional datasets, including third-order tensor, fourth-order tensor, and fifth-order tensor, to evaluate the proposed method's generalization capabilities. Experimental results demonstrate that the proposed MPCP method significantly outperforms the state-of-the-art methods. A dedicated comparative analysis against MCP-based variants further reveals the MPCP method's superior performance, thereby corroborating our theoretical analysis.

The rest of the paper is organized as follows. In Section 2, some preliminary knowledge and background of the tensors are given. Definitions and theorems about the MPCP function are presented in Section 3. The main results, including the proposed model and algorithm, are shown in Section 4. In Section 5, we give the convergency analysis for the proposed method. The results of extensive experiments and discussion are presented in Section 6. Conclusions are drawn in Section 7.

2 Preliminaries

In this section, we give some basic notations and briefly introduce some definitions used throughout the paper. Generally, a lowercase letter and an uppercase letter denote a vector b and a matrix B , respectively. A calligraphic upper case letter $\mathcal{B} \in \mathbb{R}^{J_1 \times J_2 \times \cdots \times J_N}$ denotes an N th-order tensor and $\mathcal{B}_{j_1, j_2, \dots, j_N}$ is its (j_1, j_2, \dots, j_N) -th element. The Frobenius norm of a tensor is defined as $\|\mathcal{B}\|_F = (\sum_{j_1, j_2, \dots, j_N} \mathcal{B}_{j_1, j_2, \dots, j_N}^2)^{1/2}$. For a third-order tensor $\mathcal{B} \in \mathbb{R}^{J_1 \times J_2 \times J_3}$, we use the Matlab notation $\mathcal{B}(k, :, :)$, $\mathcal{B}(:, i, :)$ and $\mathcal{B}(:, :, j) := \mathcal{B}^{(j)}$ to denote its k th horizontal slice, i th lateral slice and j th frontal slice, respectively, and $\mathcal{B}(k, i, :)$ is denoted (k, i) -th tube of \mathcal{B} .

Definition 2.1 (Tensor mode- n unfolding and folding [14]). The mode- n unfolding of an N th-order tensor $\mathcal{B} \in \mathbb{R}^{J_1 \times J_2 \times \cdots \times J_N}$ is denoted as a matrix $\mathcal{B}_{(n)} \in \mathbb{R}^{J_n \times J_1 \cdots J_{n-1} J_{n+1} \cdots J_N}$. Tensor element (j_1, j_2, \dots, j_N) maps to matrix element (j_n, l) , where

$$l = 1 + \sum_{i=1, i \neq n}^N (j_i - 1)L_i \quad \text{with} \quad L_i = \prod_{k=1, k \neq n}^{i-1} J_k.$$

The mode- n unfolding operator and its inverse are respectively denoted as unfold_n and fold_n , and they satisfy $\mathcal{B} = \text{fold}_n(\mathcal{B}_{(n)}) = \text{fold}_n(\text{unfold}_n(\mathcal{B}))$.

Definition 2.2 (The mode- n product of tensor [14]). The mode- n product of an N th-order tensor $\mathcal{B} \in \mathbb{R}^{J_1 \times J_2 \times \cdots \times J_N}$ with matrix $M \in \mathbb{R}^{I_n \times J_n}$ is denoted by $\mathcal{C} = \mathcal{B} \times_n M$. Elementwise, we have

$$\mathcal{C} = \mathcal{B} \times_n M \in \mathbb{R}^{J_1 \times J_2 \times \cdots \times J_{n-1} \times I_n \times J_{n+1} \times \cdots \times J_N} \quad \Leftrightarrow \quad \mathcal{C}_{(n)} = M \mathcal{B}_{(n)}.$$

Now we review the Discrete Fourier Transformation (DFT) for tensor-tensor product. For a third-order tensor $\mathcal{B} \in \mathbb{C}^{J_1 \times J_2 \times J_3}$, let $\bar{\mathcal{B}} \in \mathbb{C}^{J_1 \times J_2 \times J_3}$ be the result of DFT of \mathcal{B} along the third mode. Specifically, let $F = [\mathbf{f}_1, \dots, \mathbf{f}_{J_3}] \in \mathbb{R}^{J_3 \times J_3}$, where $\mathbf{f}_k =$

$[\omega^{0 \times (k-1)}; \dots; \omega^{(J_3-1) \times (k-1)}] \in \mathbb{R}^{J_3}$, $\omega = e^{-\frac{2\pi t}{J_3}}$ and $t = \sqrt{-1}$. Then $\bar{\mathcal{B}}(k, i, :) = F\mathcal{B}(k, i, :)$, which can be computed by Matlab command $\bar{\mathcal{B}} = \text{fft}(\mathcal{B}, [], 3) = \mathcal{B} \times_3 F$. Furthermore, the inverse DFT is computed by command ifft satisfying $\mathcal{B} = \text{ifft}(\bar{\mathcal{B}}, [], 3)$. For a third-order tensor $\mathcal{B} \in \mathbb{R}^{J_1 \times J_2 \times J_3}$, the block circulation operation is defined as

$$\text{bcirc}(\mathcal{B}) := \begin{pmatrix} \mathcal{B}^{(1)} & \mathcal{B}^{(J_3)} & \dots & \mathcal{B}^{(2)} \\ \mathcal{B}^{(2)} & \mathcal{B}^{(1)} & \dots & \mathcal{B}^{(3)} \\ \vdots & \vdots & \ddots & \vdots \\ \mathcal{B}^{(J_3)} & \mathcal{B}^{(J_3-1)} & \dots & \mathcal{B}^{(1)} \end{pmatrix} \in \mathbb{R}^{J_1 J_3 \times J_2 J_3}.$$

The block diagonalization operation and its inverse operation are respectively defined as $\text{bdiag}(\mathcal{B}) := \text{diag}(\mathcal{B}^{(1)}, \mathcal{B}^{(2)}, \dots, \mathcal{B}^{(J_3)}) \in \mathbb{R}^{J_1 J_3 \times J_2 J_3}$ and $\text{bdfold}(\text{bdiag}(\mathcal{B})) := \mathcal{B}$. The block vectorization operation and its inverse operation are respectively defined as

$$\text{bvec}(\mathcal{B}) := \begin{pmatrix} \mathcal{B}^{(1)} \\ \mathcal{B}^{(2)} \\ \vdots \\ \mathcal{B}^{(J_3)} \end{pmatrix} \in \mathbb{R}^{J_1 J_3 \times J_2} \text{ and } \text{bvfold}(\text{bvec}(\mathcal{B})) := \mathcal{B}.$$

Definition 2.3 (T-product [12]). Let $\mathcal{B} \in \mathbb{R}^{J_1 \times J_2 \times J_3}$ and $\mathcal{C} \in \mathbb{R}^{J_2 \times I \times J_3}$. The t-product $\mathcal{B} * \mathcal{C}$ is defined to be a tensor of size $J_1 \times I \times J_3$,

$$\mathcal{B} * \mathcal{C} := \text{bvfold}(\text{bcirc}(\mathcal{B})\text{bvec}(\mathcal{C})).$$

Since that the circular convolution in the spatial domain is equivalent to the element-wise multiplication in the Fourier domain, the t-product between two tensors $\mathcal{C} = \mathcal{A} * \mathcal{B}$ is equivalent to $\bar{\mathcal{C}} = \text{bdfold}(\text{bdiag}(\bar{\mathcal{A}})\text{bdiag}(\bar{\mathcal{B}}))$.

The conjugate transpose of a tensor $\mathcal{B} \in \mathbb{C}^{J_1 \times J_2 \times J_3}$ is the tensor $\mathcal{B}^H \in \mathbb{C}^{J_2 \times J_1 \times J_3}$ [12] obtained by conjugate transposing each of the frontal slices and then reversing the order of transposed frontal slices 2 through J_3 . Besides, the identity tensor $\mathcal{I} \in \mathbb{R}^{J_1 \times J_1 \times J_3}$ is the tensor whose first frontal slice is the $J_1 \times J_1$ identity matrix, and whose other frontal slices are all zeros. It is easy to get $\mathcal{B} * \mathcal{I} = \mathcal{B} = \mathcal{I} * \mathcal{B}$. A tensor $\mathcal{Q} \in \mathbb{R}^{J_1 \times J_1 \times J_3}$ is orthogonal if it satisfies $\mathcal{Q} * \mathcal{Q}^H = \mathcal{Q}^H * \mathcal{Q} = \mathcal{I}$. A third-order tensor is called f-diagonal if each of its frontal slices is a diagonal matrix.

Lemma 2.1 (T-SVD [16]). Let $\mathcal{B} \in \mathbb{R}^{J_1 \times J_2 \times J_3}$ be a third-order tensor, then it can be factored as

$$\mathcal{B} = \mathcal{U} * \mathcal{S} * \mathcal{V}^H,$$

where $\mathcal{U} \in \mathbb{R}^{J_1 \times J_1 \times J_3}$ and $\mathcal{V} \in \mathbb{R}^{J_2 \times J_2 \times J_3}$ are orthogonal tensors, and $\mathcal{S} \in \mathbb{R}^{J_1 \times J_2 \times J_3}$ is an f-diagonal tensor.

Definition 2.4 (Tensor tubal rank [33]). The tubal rank of a tensor $\mathcal{B} \in \mathbb{R}^{J_1 \times J_2 \times J_3}$, denoted as $\text{rank}_t(\mathcal{B})$, is defined to be the number of non-zero singular tubes of \mathcal{S} , where \mathcal{S} comes from the t-SVD of $\mathcal{B} : \mathcal{B} = \mathcal{U} * \mathcal{S} * \mathcal{V}^H$. That is $\text{rank}_t(\mathcal{B}) = \#\{j : \mathcal{S}(j, j, :) \neq 0\}$.

Definition 2.5 (Tensor nuclear norm (TNN)). The tensor nuclear norm of a tensor $\mathcal{B} \in \mathbb{R}^{J_1 \times J_2 \times J_3}$, denoted as $\|\mathcal{B}\|_{TNN}$, is defined as the sum of the singular values of all the frontal slices of $\bar{\mathcal{B}}$, i.e.,

$$\|\mathcal{B}\|_{TNN} := \frac{1}{J_3} \sum_{j=1}^{J_3} \|\bar{\mathcal{B}}^{(j)}\|_* = \frac{1}{J_3} \sum_{j=1}^{J_3} \sum_{i=1}^R \sigma_i(\bar{\mathcal{B}}^{(j)}),$$

where $\bar{\mathcal{B}}^{(j)}$ is the j -th frontal slice of $\bar{\mathcal{B}}$, with $\bar{\mathcal{B}} = \text{fft}(\mathcal{B}, [], 3)$; $R = \min(J_1, J_2)$; $\sigma_j(\bar{\mathcal{B}}^{(j)})$ is the i -th singular value of $\bar{\mathcal{B}}^{(j)}$.

In order to simplify the representation of the correlation between pairs of dimensions of a tensor, a new tensor mode- q unfolding and folding definition has been proposed to replace the tensor mode- k_1, k_2 unfolding and folding definition in [39].

Definition 2.6 (Tensor mode- q unfolding and folding). For an N th-order tensor \mathcal{B} , its mode- q unfolding is a third-order tensor denoted by $\mathcal{B}_{<q>} \in \mathbb{R}^{J_{q_1} \times J_{q_2} \times \prod_{s \neq q_1, q_2} J_s}$. Mathematically, the (j_1, j_2, \dots, j_N) -th element of \mathcal{B} maps to the (j_{q_1}, j_{q_2}, k) -th element of $\mathcal{B}_{<q>}$, where

$$k = 1 + \sum_{s=1, s \neq q_1, q_2}^N (j_s - 1) \prod_{m=1, m \neq q_1, q_2}^{s-1} J_m,$$

$$q = (q_1 - 1)(N - q_1/2) + q_2 - q_1, \quad 1 \leq q_1 < q_2 \leq N.$$

The mode- q unfolding operator and its inverse operation are respectively denoted as $\mathcal{B}_{<q>} := \text{t-unfold}(\mathcal{B}, q)$ and $\mathcal{B} := \text{t-fold}(\mathcal{B}_{<q>}, q)$. Additionally, q ranges from 1 to $N(N-1)/2$.

Definition 2.7 (N-tubal rank [39]). The N-tubal rank of an N th-order tensor \mathcal{B} is defined as a vector, the elements of which contain the tubal rank of all mode- q unfolding tensors, i.e.,

$$N - \text{rank}_t(\mathcal{B}) := (\text{rank}_t(\mathcal{B}_{<1>}), \text{rank}_t(\mathcal{B}_{<2>}), \dots, \text{rank}_t(\mathcal{B}_{<N(N-1)/2>})) \in \mathbb{R}^{N(N-1)/2}.$$

Definition 2.8 (MCP function [38]). Let $\tau > 1$. The MCP function $h_\tau : \mathbb{R} \rightarrow \mathbb{R}_{\geq 0}$ is defined as

$$h_\tau(x) = \begin{cases} |x| - \frac{x^2}{2\tau}, & |x| \leq \tau, \\ \frac{\tau}{2}, & |x| > \tau, \end{cases} \quad (1)$$

where $\mathbb{R}_{\geq 0}$ denotes the domain of non-negative real numbers.

Based on the definition of the MCP function, it can be observed that the function controls the penalty threshold in the LRTPC problem by adjusting the τ value. As τ increases, the penalty on small singular values gradually intensifies, but the protection range for large singular values narrows. Conversely, decreasing τ can expand the protection range for large singular values, but it weakens the penalty on small singular values.

3 Minimax p -th order concave penalty function

In this section, to address the limitations of the MCP function, the definition of the MPCP function is proposed.

Definition 3.1 (MPCP function). Let $\tau > 1$, $0 < p < 1$. The MPCP function $\psi_{\tau,p} : \mathbb{R} \rightarrow \mathbb{R}_{\geq 0}$ is defined as

$$\psi_{\tau,p}(x) = \begin{cases} |x| - \frac{|x|^{1+p}}{(1+p)\tau}, & |x| \leq \tau^{1/p}, \\ \frac{p\tau^{1/p}}{1+p}, & |x| > \tau^{1/p}. \end{cases} \quad (2)$$

Compared to the MCP function, the proposed MPCP function introduces an additional p parameter. It is evident that when $p = 1$, the MPCP function is identical to the MCP function, while for $p < 1$, there is a clear difference between the MPCP function and the MCP function. This indicates that the MPCP function has a broader definition than the MCP function. Additionally, the MPCP function can enhance the penalty on small singular values by decreasing the p value. Fig. 1 shows the function plot for the MCP function with $\tau = 2$, as well as the function plots for the MPCP function with p values ranging from 0.1 to 0.9 and $\tau = 2^{1/p}$. All plots have the boundary at $x = \pm 2$. From the figure, it is clear that as the p value decreases, the penalty on x increases, which demonstrates that the MPCP function can impose a stronger penalty on small singular values compared to the MCP function in the LRTC problem. In the LRTC problem, larger singular values typically represent important information, such as contours and smooth regions, while smaller singular values are primarily composed of noise or outliers [3]. Therefore, protecting large singular values and enhancing the penalty on smaller singular values are both crucial for ensuring recovery performance and improving image restoration. The MPCP function effectively possesses both of these properties. Additionally, we further analyzed some properties of the MPCP function. Since the MPCP function is symmetric function, it is sufficient to analyze its properties on $[0, +\infty)$.

Theorem 3.1. The MPCP function defined in (2) satisfies the following properties:

1. $\psi_{\tau,p}(x)$ is continuous, smooth on $[0, +\infty)$ and $\psi_{\tau,p}(0) = 0$, $\lim_{x \rightarrow +\infty} \frac{\psi_{\tau,p}(x)}{x} = 0$;
2. $\psi_{\tau,p}(x)$ is monotonically non-decreasing and concave on $[0, +\infty)$;
3. $\psi_{\tau,p}(x)$ is subadditive;
4. $\psi'_{\tau,p}(x)$ is non-negativity and monotonicity non-increasing on $[0, +\infty)$. Moreover, it is Lipschitz bounded, i.e., there exists constant $L(\ell)$ such that

$$|\psi'_{\tau,p}(x) - \psi'_{\tau,p}(y)| \leq L(\ell)|x - y|;$$

5. Especially, for the MPCP function, it is increasing as the parameter τ increases, and

$$\lim_{\tau \rightarrow +\infty} \psi_{\tau,p}(x) = |x|,$$

which indicates that as the parameter τ increases, the MPCP function becomes closer to $|x|$.

Proof. 1. $\lim_{-} \psi_{\tau,p}(\tau^{1/p}) = \lim_{+} \psi_{\tau,p}(\tau^{1/p}) = p\tau^{1/p}/(1+p)$ and $\psi'_{-\tau,p}(\tau^{1/p}) = \psi'_{+\tau,p}(\tau^{1/p}) = 0$, thus it's continuous and smooth; At last, the conclusions $\psi_{\tau,p}(0) = 0$ and $\lim_{x \rightarrow +\infty} \frac{\psi_{\tau,p}(x)}{x} = 0$ are easily to verified though the formulas in (2).

2. This conclusion is direct from its first order and second order derivative function. Its first order and second order derivative functions are as follows:

$$\psi'_{\tau,p}(x) = \begin{cases} 1 - \frac{|x|^p}{\tau}, & |x| \leq \tau^{1/p}, \\ 0, & |x| > \tau^{1/p}. \end{cases} \quad (3)$$

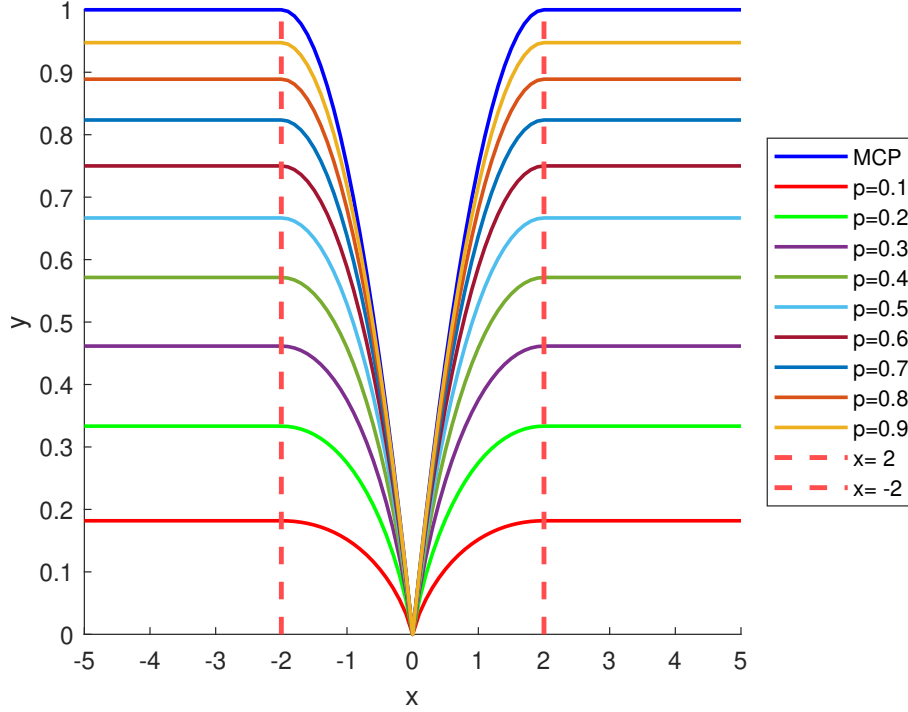


Figure 1: Plots for $x = 2$, $x = -2$, the MCP and MPCP functions. Here $\tau = 2$ for the MCP function; $p = \{0.1, 0.2, \dots, 0.9\}$, $\tau = 2^{1/p}$ for the MPCP function.

$$\psi''_{\tau,p}(x) = \begin{cases} -\frac{p|x|^{p-1}}{\tau}, & |x| \leq \tau^{1/p}, \\ 0, & |x| > \tau^{1/p}. \end{cases} \quad (4)$$

It can be find that its first order derivative function is non-negative and its second order derivative function is non-positive, thus $\psi_{\tau,p}(x)$ is concave and monotonically non-decreasing on $[0, +\infty)$.

3. For $x_1 \geq 0$ and $x_2 \geq 0$, concavity implies

$$\psi_{\tau,p}(x_1) = \psi_{\tau,p}\left(\frac{x_1}{x_1+x_2}(x_1+x_2) + \frac{x_2}{x_1+x_2}0\right) \geq \frac{x_1}{x_1+x_2}\psi_{\tau,p}(x_1+x_2) + \frac{x_2}{x_1+x_2}\psi_{\tau,p}(0),$$

and

$$\psi_{\tau,p}(x_2) = \psi_{\tau,p}\left(\frac{x_2}{x_1+x_2}(x_1+x_2) + \frac{x_1}{x_1+x_2}0\right) \geq \frac{x_2}{x_1+x_2}\psi_{\tau,p}(x_1+x_2) + \frac{x_1}{x_1+x_2}\psi_{\tau,p}(0).$$

Then,

$$\psi_{\tau,p}(x_1) + \psi_{\tau,p}(x_2) \geq \psi_{\tau,p}(x_1+x_2) + \psi_{\tau,p}(0) = \psi_{\tau,p}(x_1+x_2).$$

4. The non-negativity and monotonicity of $\psi'_{\tau,p}(x)$ is direct from the formulas presented in (3). Next, we verify its Lipschitz bounded. The proof is mainly based on that $\psi''_{\tau,p}(x) \leq 0$ and monotonically non-decreasing on $(0, +\infty)$, which turns that $\psi''_{\tau,p}(x)$ is always bounded. Thus exists constant $L(\ell) := \max\{\psi''_{\tau,p}(x), \psi''_{\tau,p}(y)\}$ for any $x, y \in (0, +\infty)$, we have

$$|\psi'_{\tau,p}(x) - \psi'_{\tau,p}(y)| \leq L(\ell)|x - y|.$$

5. Consider $\psi_{\tau,p}(x)$ is a function with respect to τ when x and p are fixed, then its derivative function is computed as follows:

$$\begin{cases} \frac{\tau^{1/p-1}}{1+p}, & \tau < |x|^p, \\ \frac{|x|^{1+p}}{(1+p)\tau^2}, & \tau \geq |x|^p. \end{cases}$$

It demonstrates that MPCP function is increasing in τ since its derivative function is non-negative. Note that as $\tau \rightarrow +\infty$,

$$|x| - \frac{|x|^{1+p}}{(1+p)\tau} \rightarrow |x|.$$

Then the limit results follow easily. This completes the proof. \square

To facilitate the application of the MPCP function in the LRTC problem, the proximal operator for the MPCP function is proposed.

Theorem 3.2 (Proximal operator for the MPCP function). Consider the MPCP function given in (2), $\tau > 1$, $1 > p > 0$. Its proximal operator is denoted by $P_\rho : \mathbb{R} \rightarrow \mathbb{R}$ and defined as follows:

$$P_\rho(y) = \arg \min_x \left\{ \frac{1}{2}(x - y)^2 + \rho\psi_{\tau,p}(x) \right\}, \quad (5)$$

which can be represented by

$$P_\rho(y) = x_1 \odot \text{sign}(y) \quad \text{with} \quad x_1 = \begin{cases} 0, & |y| < h_a, \\ x_a, & |y| = h_a, \\ x_*, & \tau^{1/p} > |y| > h_a, \\ |y|, & |y| \geq \tau^{1/p}, \end{cases} \quad (6)$$

where $x_a = (\frac{2\rho p}{(1+p)\tau})^{\frac{1}{1-p}}$, $h_a = x_a - \rho x_a^p / \tau + \rho$, \odot is hadamard product. For $|y| > h_a$, $x_* \in (x_a, |y|)$ solves:

$$x - \rho x^p / \tau + \rho = |y| \quad \text{where} \quad x > 0. \quad (7)$$

When $|y| > h_a$, there are two solutions to (7) and x_* is the larger one which can be computed from the iteration:

$$x_{k+1} = \alpha(x_k) \quad \text{where} \quad \alpha(x) = |y| - \rho + \rho x^p / \tau, \quad (8)$$

with the initial condition $x_0 \in [x_a, |y|]$.

Proof. According to the definition of $\psi_{\tau,p}(x)$, when $|x| \geq \tau^{1/p}$, $P_\rho(y) = y$, and $|y| = 0$, $P_\rho(y) = 0$. Next, we consider the case $0 < |x| < \tau^{1/p}$. Since x and y have the same sign and $\psi_{\tau,p}(x)$ is a symmetric function, it is sufficient to consider only the case where $y > 0$ and $x > 0$. Let $g(x) = \frac{1}{2}(x - y)^2 + \rho(x - \frac{x^{1+p}}{(1+p)\tau})$. Noting that $g(0) = \frac{y^2}{2}$. As $g(x)$ is differentiable for $\tau^{1/p} \geq x > 0$, re-arranging $g'(x) = 0$ gives:

$$m(x) := x + \rho - \rho \frac{x^p}{\tau} = y. \quad (9)$$

Now, note that $m(x)$ has a minimum where $m'(x) = 0$, i.e., where $1 - \frac{\rho p}{\tau} x^{p-1} = 0$ giving $x = x_b = (\frac{\rho p}{\tau})^{\frac{1}{1-p}}$. Further, $m''(x) = \frac{(1-p)\rho p}{\tau} x^{p-2} > 0$ for all $\tau^{1/p} \geq x > 0$. So m has a global minimum of value $h_b = x_b + \rho - \rho \frac{x_b^p}{\tau}$. Thus (9) no solution unless $y \geq h_b$, see Fig. 2. Further, $m'(x) < 0$ for $x < x_b$ (m is strictly decreasing for $x < x_b$), while $m'(x) > 0$ for $x > x_b$ (m is strictly increasing for $x > x_b$). So (9) has at least one solution for $y \geq h_b$. Once again, for the illustration see Fig. 2. Further, suppose x_* is a solution to (9). Then

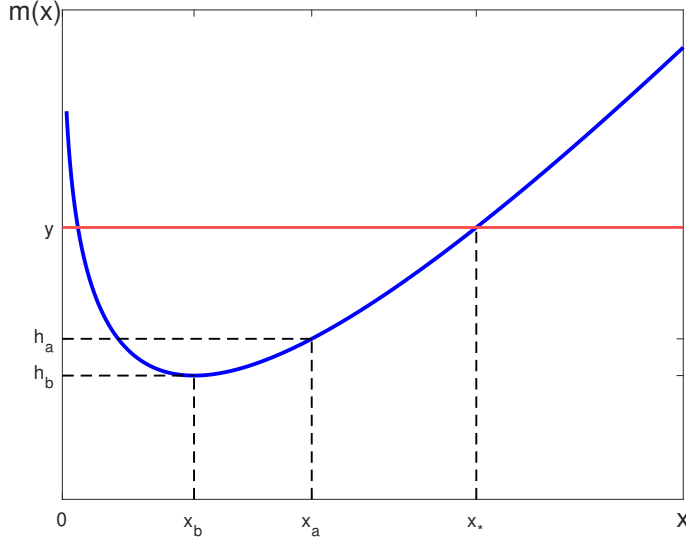


Figure 2: Plot for $m(x)$ for $x > 0$.

the corresponding value of g is:

$$\begin{aligned}
 g(x_*) &= \frac{1}{2}y^2 - yx_* + \frac{1}{2}x_*^2 + \rho(x_* - \frac{x_*^{1+p}}{(1+p)\tau}) \\
 &= g(0) + \frac{1}{2}x_*^{1+p}(x_*^{1-p} + 2(\rho - y)x_*^{-p} - \frac{2\rho}{(1+p)\tau}) \\
 &= g(0) + \frac{1}{2}x_*^{1+p}(\frac{2\rho p}{(1+p)\tau} - x_*^{1-p}) \\
 &= g(0) + \frac{1}{2}x_*^{1+p}(x_a^{1-p} - x_*^{1-p}),
 \end{aligned}$$

which implies that $g(x_*) \leq g(0)$ if $x_* \geq x_a$. So for a non-zero solution we are only interested in $x_* > x_a$, and $x_a > x_b$, it can be seen in Fig. 2, this is the larger solution to (9).

Lastly, as $m(x)$ is strictly increasing for $x > x_b$ we have that $x_* \geq x_a$ is equivalent to $y \geq h_a$. This can also be seen in Fig. 2. We thus conclude that the global minimizer of $g(x)$ is as stated in the theorem.

The iterations using (8) only need to be applied when $\tau^{1/p} > |y| > h_a$. For the case $|y| = h_a$ we already have that $x_* = x_a$. As a result, we take $\tau^{1/p} > |y| > h_a$ and firstly show that:

$$\alpha([x_a, |y|]) \subset [x_a, |y|]. \quad (10)$$

Let $x \in [x_a, |y|]$. Then as $x \geq x_a > 0$, by definition of α we have $\alpha(x) < |y|$, and by definition of h_a we also have $h_a \geq x_a + \rho - \rho x^p/\tau$. This last inequality and $|y| > h_a$ imply $|y| > x_a + \rho - \rho x^p/\tau$, which by re-arrangement and definition of α gives $\alpha(x) > x_a$. Therefore, $x_a < \alpha(x) < |y|$, which proves (10).

Next, we show that α is a contraction mapping on $[x_a, |y|]$. By differentiating we have $\alpha'(x) = p\rho x^{p-1}/\tau$, and obviously $\alpha'(x) > 0$ as $x \geq x_a > 0$ i.e., α' is positive on $[x_a, |y|]$. Then by re-arranging α' it can easily be deduced that: $\alpha'(x) < 1$ iff $x > x_b$. Since $x \geq x_a > x_b$ we have that $\alpha'(x) < 1$. Therefore, α is a contraction on $[x_a, |y|]$.

Lastly, as \mathbb{R} is complete and $[x_a, |y|] \subset \mathbb{R}$ is closed implies $[x_a, |y|]$ is also complete. Then by the standard Banach fixed point theorem: α admits one and only one fixed point $x_{\dagger} \in [x_a, |y|]$, i.e., $x_{\dagger} = |y| - \rho + \rho x_{\dagger}^p/\tau$. Since $x_{\star} \in (x_a, |y|) \subset [x_a, |y|]$ satisfies the fixed point equation we must have $x_{\dagger} = x_{\star}$. \square

For the tensor case, the tensor p -th order τ norm is proposed, and its properties are analyzed.

Definition 3.2 (Tensor p -th order τ norm). The tensor p -th order τ norm of $\mathcal{B} \in \mathbb{R}^{J_1 \times J_2 \times J_3}$, denoted by $\|\mathcal{B}\|_{\tau p}$, is defined as follows:

$$\|\mathcal{B}\|_{\tau p} = \frac{1}{J_3} \sum_{j=1}^{J_3} \|\bar{\mathcal{B}}^{(j)}\|_{\tau p} = \frac{1}{J_3} \sum_{j=1}^{J_3} \sum_{i=1}^R \psi_{\tau, p}(\sigma_i(\bar{\mathcal{B}}^{(j)})), \quad (11)$$

where $\tau > 1, 1 > p > 0$; $\bar{\mathcal{B}}^{(j)}$ is the j -th frontal slice of $\bar{\mathcal{B}}$, with $\bar{\mathcal{B}} = \text{fft}(\mathcal{B}, [\], 3)$; $R = \min(J_1, J_2)$; $\sigma_i(\bar{\mathcal{B}}^{(j)})$ is the i -th singular value of $\bar{\mathcal{B}}^{(j)}$.

Unlike the tensor nuclear norm, the tensor p -th order τ norm is not a true norm, as it does not satisfy homogeneity. Therefore, the term “norm” is used merely as a naming convention. Below, some important properties satisfied by the tensor p -th order τ norm are presented.

Theorem 3.3. The tensor p -th order τ norm defined in (11) satisfies the following properties:

- 1. Non-negativity:** The tensor p -th order τ norm is non-negative, i.e., $\|\mathcal{B}\|_{\tau p} \geq 0$. The equality holds if and only if \mathcal{B} is the null tensor.
- 2. Unitary invariance:** The tensor p -th order τ norm is unitary invariant, i.e., $\|\mathcal{U} * \mathcal{B} * \mathcal{V}\|_{\tau p} = \|\mathcal{B}\|_{\tau p}$, for unitary tensor \mathcal{U} and \mathcal{V} .
- 3. Triangle inequality:** Suppose that $\mathcal{C} \in \mathbb{R}^{J_1 \times J_2 \times J_3}$ and $\mathcal{D} \in \mathbb{R}^{J_1 \times J_2 \times J_3}$ are two arbitrary tensors. Then, the following properties hold: $\|\mathcal{C} - \mathcal{D}\|_{\tau p} \geq \|\mathcal{C}\|_{\tau p} - \|\mathcal{D}\|_{\tau p}$.

Before we proof Theorem 3.3, we first present a lemma.

Lemma 3.1 ([24], Theorem 1). Suppose that C and D are two same-sized matrices and that $\psi(x)$ satisfies Theorem 3.1 (i). Then $\|C + D\|_{\tau p} \leq \|C\|_{\tau p} + \|D\|_{\tau p}$.

Then we proceed to prove Theorem 3.3.

Proof. 1. Since $\|\mathcal{B}\|_{\tau p}$ is the sum of non-negative functions $\psi_{\tau, p}(\sigma_i(\bar{\mathcal{B}}^{(j)}))$, $\|\mathcal{B}\|_{\tau p}$ is non-negative, i.e., $\|\mathcal{B}\|_{\tau p} \geq 0$.

2. Considering the definition of the tensor p -th order τ norm, $\|\mathcal{B}\|_{\tau p}$ can be expressed as follows:

$$\|\mathcal{B}\|_{\tau p} = \frac{1}{J_3} \sum_{j=1}^{J_3} \text{Tr}(\psi_{\tau,p}(\sqrt{\bar{\mathcal{B}}^{(j)T} \bar{\mathcal{B}}^{(j)}})),$$

where $\text{Tr}(\cdot)$ denotes the trace operator, $\psi_{\tau,p}(\cdot)$ means to take the MPCP function of each element. Next, consider $\|\mathcal{U} * \mathcal{B} * \mathcal{V}\|_{\tau p}$, where \mathcal{U} and \mathcal{V} are unitary tensors:

$$\|\mathcal{U} * \mathcal{B} * \mathcal{V}\|_{\tau p} = \frac{1}{J_3} \sum_{j=1}^{J_3} \text{Tr}(\psi_{\tau,p}(\sqrt{(\bar{\mathcal{U}}^{(j)} \bar{\mathcal{B}}^{(j)} \bar{\mathcal{V}}^{(j)})^T \bar{\mathcal{U}}^{(j)} \bar{\mathcal{B}}^{(j)} \bar{\mathcal{V}}^{(j)}})).$$

Properties of the tensor generated by performing DFT show that $\bar{\mathcal{U}}^{(j)}$ and $\bar{\mathcal{V}}^{(j)}$ are unitary matrix. Then, we get the following formula:

$$\|\mathcal{U} * \mathcal{B} * \mathcal{V}\|_{\tau p} = \|\mathcal{B}\|_{\tau p}.$$

This establishes the invariance of the tensor p -th order τ norm to unitary transformations.

3. Denote $\mathcal{A} = \mathcal{C} - \mathcal{D}$. By Lemma 3.1, we obtain that

$$\begin{aligned} \|\mathcal{C}\|_{\tau p} &= \|\mathcal{A} + \mathcal{D}\|_{\tau p} \\ &= \frac{1}{J_3} \sum_{j=1}^{J_3} \|\bar{\mathcal{A}}^{(j)} + \bar{\mathcal{D}}^{(j)}\|_{\tau p} \\ &\leq \frac{1}{J_3} \sum_{j=1}^{J_3} \|\bar{\mathcal{A}}^{(j)}\|_{\tau p} + \frac{1}{J_3} \sum_{j=1}^{J_3} \|\bar{\mathcal{D}}^{(j)}\|_{\tau p} \\ &= \|\mathcal{A}\|_{\tau p} + \|\mathcal{D}\|_{\tau p}, \end{aligned}$$

which implies that $\|\mathcal{C} - \mathcal{D}\|_{\tau p} \geq \|\mathcal{C}\|_{\tau p} - \|\mathcal{D}\|_{\tau p}$. \square

Additionally, to facilitate the solution of subsequent algorithms, the proximal operator for the tensor p -th order τ norm is proposed.

Theorem 3.4 (Proximal operator for the tensor p -th order τ norm). Consider the tensor p -th order τ norm given in (11). Its proximal operator is denoted by $S_\rho : \mathbb{R}^{J_1 \times J_2 \times J_3} \rightarrow \mathbb{R}^{J_1 \times J_2 \times J_3}$, $0 < p < 1$, $\tau > 1$, $R = \min\{J_1, J_2\}$ and defined as follows:

$$S_\rho(\mathcal{Y}) = \arg \min_{\mathcal{B}} \frac{1}{2} \|\mathcal{B} - \mathcal{Y}\|_F^2 + \rho \|\mathcal{B}\|_{\tau p} \quad (12)$$

is given by

$$S_\rho(\mathcal{Y}) = \mathcal{M} * \mathcal{S}_1 * \mathcal{Q}^H, \quad (13)$$

where \mathcal{M} and \mathcal{Q} are derived from the t-SVD of $\mathcal{Y} = \mathcal{M} * \mathcal{S}_2 * \mathcal{Q}^H$. Additionally, the (k, k) -th elements of the j -th frontal slice of $\bar{\mathcal{S}}_1$ and $\bar{\mathcal{S}}_2$ are $\sigma_k(\bar{\mathcal{B}}^{(j)})$ and $\sigma_k(\bar{\mathcal{Y}}^{(j)})$, i.e., $\bar{\mathcal{S}}_1^{(j)}(k, k) = \sigma_k(\bar{\mathcal{B}}^{(j)})$ and $\bar{\mathcal{S}}_2^{(j)}(k, k) = \sigma_k(\bar{\mathcal{Y}}^{(j)})$, respectively. More importantly, $\sigma_k(\bar{\mathcal{B}}^{(j)})$ and $\sigma_k(\bar{\mathcal{Y}}^{(j)})$ have the following relationship $\sigma_k(\bar{\mathcal{B}}^{(j)}) = P_\rho(\sigma_k(\bar{\mathcal{Y}}^{(j)}))$.

Proof. Let $\mathcal{Y} = \mathcal{M} * \mathcal{S}_2 * \mathcal{Q}^H$ and $\mathcal{B} = \mathcal{U} * \mathcal{S}_1 * \mathcal{V}^H$ be the t-SVD of \mathcal{Y} and \mathcal{B} , respectively. Consider

$$\begin{aligned}
S_\rho(\mathcal{Y}) &= \arg \min_{\mathcal{B}} \frac{1}{2} \|\mathcal{B} - \mathcal{Y}\|_F^2 + \rho \|\mathcal{B}\|_{\tau p} \\
&= \arg \min_{\mathcal{B}} \frac{1}{2} \|\mathcal{U} * \mathcal{S}_1 * \mathcal{V}^H - \mathcal{M} * \mathcal{S}_2 * \mathcal{Q}^H\|_F^2 + \rho \|\mathcal{B}\|_{\tau p} \\
&= \arg \min_{\mathcal{B}} \frac{1}{J_3} \sum_{j=1}^{J_3} \left(\frac{1}{2} \|\bar{\mathcal{U}}^{(j)} * \bar{\mathcal{S}}_1^{(j)} * \bar{\mathcal{V}}^{(j)H} - \bar{\mathcal{M}}^{(j)} * \bar{\mathcal{S}}_2^{(j)} * \bar{\mathcal{Q}}^{(j)H}\|_F^2 + \rho \|\bar{\mathcal{B}}^{(j)}\|_{\tau p} \right).
\end{aligned} \tag{14}$$

It can be found that (14) is separable and can be divided into J_3 sub-problems. For the j -th sub-problem:

$$\begin{aligned}
&\arg \min_{\bar{\mathcal{B}}^{(j)}} \frac{1}{2} \|\bar{\mathcal{U}}^{(j)} * \bar{\mathcal{S}}_1^{(j)} * \bar{\mathcal{V}}^{(j)H} - \bar{\mathcal{M}}^{(j)} * \bar{\mathcal{S}}_2^{(j)} * \bar{\mathcal{Q}}^{(j)H}\|_F^2 + \rho \|\bar{\mathcal{B}}^{(j)}\|_{\tau p} \\
&= \arg \min_{\bar{\mathcal{B}}^{(j)}} \frac{1}{2} \text{Tr}(\bar{\mathcal{S}}_1^{(j)} \bar{\mathcal{S}}_1^{(j)H}) + \frac{1}{2} \text{Tr}(\bar{\mathcal{S}}_2^{(j)} \bar{\mathcal{S}}_2^{(j)H}) - \text{Tr}(\bar{\mathcal{B}}^{(j)H} \bar{\mathcal{Y}}^{(j)}) + \rho \|\bar{\mathcal{B}}^{(j)}\|_{\tau p}.
\end{aligned}$$

Invoking von Neumann's trace inequality [20], we can write

$$\begin{aligned}
&\arg \min_{\bar{\mathcal{B}}^{(j)}} \frac{1}{2} \|\bar{\mathcal{U}}^{(j)} * \bar{\mathcal{S}}_1^{(j)} * \bar{\mathcal{V}}^{(j)H} - \bar{\mathcal{M}}^{(j)} * \bar{\mathcal{S}}_2^{(j)} * \bar{\mathcal{Q}}^{(j)H}\|_F^2 + \rho \|\bar{\mathcal{B}}^{(j)}\|_{\tau p} \\
&\geq \arg \min_{\bar{\mathcal{B}}^{(j)}} \frac{1}{2} \text{Tr}(\bar{\mathcal{S}}_1^{(j)} \bar{\mathcal{S}}_1^{(j)H}) + \frac{1}{2} \text{Tr}(\bar{\mathcal{S}}_2^{(j)} \bar{\mathcal{S}}_2^{(j)H}) - \text{Tr}(\bar{\mathcal{S}}_2^{(j)} \bar{\mathcal{S}}_1^{(j)H}) + \rho \|\bar{\mathcal{B}}^{(j)}\|_{\tau p} \\
&= \sum_{k=1}^R \arg \min_{\sigma_k(\bar{\mathcal{B}}^{(j)})} \frac{1}{2} (\sigma_k(\bar{\mathcal{B}}^{(j)}) - \sigma_k(\bar{\mathcal{Y}}^{(j)}))^2 + \rho \psi_{\tau, p}(\sigma_k(\bar{\mathcal{B}}^{(j)})).
\end{aligned} \tag{15}$$

The equality holds when $\bar{\mathcal{U}}^{(j)} = \bar{\mathcal{M}}^{(j)}$ and $\bar{\mathcal{V}}^{(j)} = \bar{\mathcal{Q}}^{(j)}$. By Theorem 3.2, the optimal solution of (15) can be obtained through $\sigma_k(\bar{\mathcal{B}}^{(j)}) = P_\rho(\sigma_k(\bar{\mathcal{Y}}^{(j)}))$. \square

Remark 3.1. The proximal operator for the tensor p -th order τ norm can also degenerate into a matrix form. When $J_3 = 1$, the proximal operator degenerates to the matrix case, where it is only necessary to compute the singular values of the matrix. This indicates that Theorem 3.4 applies not only to the third-order tensor case but also to the second-order matrix case.

4 MPCP-based models and solving algorithm

The LRTC problem aims at estimating the missing elements from an incomplete observed tensor. Considering an N th-order observed tensor $\mathcal{O} \in \mathbb{R}^{J_1 \times J_2 \times \dots \times J_N}$, the LRTC problem is

$$\min_{\mathcal{B}} \text{rank}(\mathcal{B}) \quad \text{s.t.} \quad \mathcal{P}_\Omega(\mathcal{B}) = \mathcal{P}_\Omega(\mathcal{O}),$$

where \mathcal{B} is the underlying tensor; the operator $\mathcal{P}_\Omega(\mathcal{B})$ function as a projection operator, retaining only the entries of \mathcal{B} that belong to Ω while setting all others to zero.

First, we use the N -tubal rank to represent the tensor rank function, then the above equation is transformed into the following form:

$$\min_{\mathcal{B}} \sum_{q=1}^{N(N-1)/2} \beta_q \mathbf{rank}_t(\mathcal{B}_{<q>}) \quad s.t. \quad \mathcal{P}_{\Omega}(\mathcal{B}) = \mathcal{P}_{\Omega}(\mathcal{O}).$$

Next, for each rank in N -tubal rank, we apply the MPCP function as the non-convex relaxation, then the proposed MPCP-based LRTC model is formulated as follow

$$\min_{\mathcal{B}} \sum_{q=1}^{N(N-1)/2} \beta_q \|\mathcal{B}_{<q>}\|_{\tau p} \quad s.t. \quad \mathcal{P}_{\Omega}(\mathcal{B}) = \mathcal{P}_{\Omega}(\mathcal{O}). \quad (16)$$

Problem (16) is difficult to optimize due to the application of multiple tensor p -th order τ norms to a tensor \mathcal{B} . Therefore, we introduce $N(N-1)/2$ auxiliary tensors $\{\mathcal{M}_q\}_{q=1}^{N(N-1)/2}$ and the indicator function $\Phi(\mathcal{B})$ to simplify this problem:

$$\min_{\mathcal{B}, \{\mathcal{M}_q\}_{q=1}^{N(N-1)/2}} \sum_{q=1}^{N(N-1)/2} \beta_q \|\mathcal{M}_{q<q>}\|_{\tau p} + \Phi(\mathcal{B}) \quad s.t. \quad \{\mathcal{M}_q = \mathcal{B}\}_{q=1}^{N(N-1)/2}, \quad (17)$$

where

$$\Phi(\mathcal{B}) := \begin{cases} 0, & \mathcal{P}_{\Omega}(\mathcal{B}) = \mathcal{P}_{\Omega}(\mathcal{O}), \\ +\infty, & \text{otherwise.} \end{cases}$$

Next, we use the ADMM [1] algorithm to solve problem (17), and its augmented Lagrangian function is as follows:

$$L(\mathcal{B}, \mathcal{M}_q, \mathcal{T}) = \sum_{q=1}^{N(N-1)/2} \beta_q \|\mathcal{M}_{q<q>}\|_{\tau p} + \langle \mathcal{B} - \mathcal{M}_q, \mathcal{T}_q \rangle + \frac{\rho_q}{2} \|\mathcal{B} - \mathcal{M}_q\|_F^2 + \Phi(\mathcal{B}), \quad (18)$$

where $\{\mathcal{T}_q\}_{q=1}^{N(N-1)/2}$ is the set of Lagrange multiplier tensors; $\{\rho_q\}_{q=1}^{N(N-1)/2} > 0$ are the augmented Lagrangian parameters; and $\beta_q \geq 0$ are weights, with $\sum_{q=1}^{N(N-1)/2} \beta_q = 1$. Accordingly, we iteratively solved the following set of subproblems within the ADMM framework:

$$\begin{cases} \mathcal{B}^{k+1} = \arg \min_{\mathcal{B}} L(\mathcal{B}, \mathcal{M}_q^k, \mathcal{T}^k), \\ \mathcal{M}_q^{k+1} = \arg \min_{\mathcal{M}_q} L(\mathcal{B}^{k+1}, \mathcal{M}_q, \mathcal{T}^k), \\ \mathcal{T}_q^{k+1} = \mathcal{T}_q^k + \rho_q^k (\mathcal{B}^{k+1} - \mathcal{M}_q^{k+1}), \end{cases} \quad (19)$$

where k represents the iteration number. Below, we provide the detailed solutions for the variables \mathcal{B} and \mathcal{M}_q .

Update \mathcal{B} : The \mathcal{B} -subproblem is a quadratic optimization problem as follows:

$$\mathcal{B}^{k+1} = \arg \min_{\mathcal{B}} \Phi(\mathcal{B}) + \sum_{q=1}^{N(N-1)/2} \frac{\rho_q^k}{2} \|\mathcal{B} - \mathcal{M}_q^k + \frac{\mathcal{T}_q^k}{\rho_q^k}\|_F^2 \quad (20)$$

$$= \mathcal{P}_{\Omega^c}((\sum_q \rho_q^k \mathcal{M}_q^k - \mathcal{T}_q^k) / \sum_q \rho_q^k) + \mathcal{P}_{\Omega}(\mathcal{O}), \quad (21)$$

where Ω^c is the complement of Ω .

Update \mathcal{M}_q : Fix other variables, and the corresponding optimization is as follows:

$$\mathcal{M}_q^{k+1} = \arg \min_{\mathcal{M}_q} \beta_q \|\mathcal{M}_{q < q >}\|_{\tau p} + \frac{\rho_q^k}{2} \|\mathcal{B}^{k+1} - \mathcal{M}_q + \frac{\mathcal{T}_q^k}{\rho_q^k}\|_F^2. \quad (22)$$

Recalling Theorem 3.4, the solution to the above optimization is given by:

$$\mathcal{M}_q^{k+1} = S_{\rho_q^k/\beta_q}(\mathcal{B}^{k+1} + \frac{\mathcal{T}_q^k}{\rho_q^k}). \quad (23)$$

The optimization steps of the MPCP formulation are outlined in Algorithm 1. The primary computational cost per-iteration arises from the update of \mathcal{M}_q , which requires the computation of t-SVD. The per-iteration complexity is $O(Y(\sum_q [\log(y_q) + \min(J_{q_1}, J_{q_2})]))$, where $Y = \prod_{j=1}^N J_j$ and $y_q = Y/(J_{q_1} J_{q_2})$. This matches the computational complexity presented in [39].

Algorithm 1 MPCP-LRTC

Input: An incomplete tensor \mathcal{O} , the index set of the known elements Ω , convergence criteria $\epsilon = 10^{-4}$, maximum iteration number K .

Initialization: $\mathcal{B}^0 = \mathcal{P}_\Omega(\mathcal{O})$, $\mathcal{Y}_q^0 = \mathcal{B}^0$, $\rho_q^0 > 0$, $\mu = 1.05$.

while not converged and $k < K$ **do**

 Updating \mathcal{B}^k via (21);

 Updating \mathcal{M}_q^k via (23);

 Updating the multipliers \mathcal{T}_q^k via (19);

$\rho_q^k = \mu \rho_q^{k-1}$, $k = k + 1$;

 Check the convergence conditions $\|\mathcal{B}^{k+1} - \mathcal{B}^k\|_F^2 / \|\mathcal{B}^k\|_F^2 \leq \epsilon$.

end while

return \mathcal{B}^{k+1} .

Output: Completed tensor \mathcal{B} .

5 Convergence analysis

In this section, to rigorously establish the theoretical convergence analysis of the proposed Algorithm 1, the following lemma is first introduced, which serves as a foundational result for the subsequent proofs and discussions.

Lemma 5.1 (Proposition 6.2 of [17]). Suppose $F : \mathbb{R}^{I_1 \times I_2} \rightarrow \mathbb{R}$ is represented as $F(X) = f \circ \sigma(X)$, where $X \in \mathbb{R}^{I_1 \times I_2}$ with SVD : $X = U \text{diag}(\sigma_1, \dots, \sigma_R) V^T$, $R = \min\{I_1, I_2\}$, and f is differentiable. The gradient of $F(X)$ at X is $\frac{\partial F(X)}{\partial X} = U \text{diag}(\theta) V^T$, $\theta = \frac{\partial f(y)}{\partial y}|_{y=\sigma(X)}$.

Lemma 5.2. The sequence $\{\mathcal{T}_q^k\}_{q=1}^{N(N-1)/2}$ generated by Algorithm 1 are bounded.

Proof. From the Lemma 5.1, for a tensor $\mathcal{Q} \in \mathbb{R}^{J_1 \times J_2 \times J_3}$, we have

$$\frac{\partial \|\bar{\mathcal{Q}}^{(j_3)}\|_{\tau p}}{\partial \bar{\mathcal{Q}}^{(j_3)}} = \bar{\mathcal{U}}^{(j_3)} \text{diag} \left(\frac{\partial \psi_{\tau,p}(\sigma_1(\bar{\mathcal{Q}}^{(j_3)}))}{\partial \sigma_1(\bar{\mathcal{Q}}^{(j_3)})}, \dots, \frac{\partial \psi_{\tau,p}(\sigma_R(\bar{\mathcal{Q}}^{(j_3)}))}{\partial \sigma_R(\bar{\mathcal{Q}}^{(j_3)})} \right) \bar{\mathcal{V}}^{(j_3)T},$$

where $R = \min\{J_1, J_2\}$. Based on the proof of Theorem 3.1, it is not difficult to obtain the following expression:

$$\frac{\partial \psi_{\tau,p}(\sigma_i(\bar{\mathcal{Q}}^{(j_3)}))}{\partial \sigma_i(\bar{\mathcal{Q}}^{(j_3)})} \leq C, \quad \forall i = 1, \dots, R, \Rightarrow \left\| \frac{\partial \|\bar{\mathcal{Q}}^{(j_3)}\|_{\tau p}}{\partial \bar{\mathcal{Q}}^{(j_3)}} \right\|_F^2 \leq RC.$$

Therefore,

$$\frac{\partial \|\bar{\mathcal{Q}}\|_{\tau p}}{\partial \bar{\mathcal{Q}}} = \left[\frac{\partial \|\bar{\mathcal{Q}}^{(1)}\|_{\tau p}}{\partial \bar{\mathcal{Q}}^{(1)}} \mid \dots \mid \frac{\partial \|\bar{\mathcal{Q}}^{(J_3)}\|_{\tau p}}{\partial \bar{\mathcal{Q}}^{(J_3)}} \right]$$

is also bounded. From $\bar{\mathcal{Q}} = \text{fft}(\mathcal{Q}, [], 3) = \mathcal{Q} \times_3 F$ and the chain rule, we conclude that

$$\|\partial_{\bar{\mathcal{Q}}} \|\mathcal{Q}\|_{\tau p}\|_F^2 = \left\| \frac{\partial \|\mathcal{Q}\|_{\tau p}}{\partial \mathcal{Q}} \right\|_F^2 = \left\| \frac{\partial \|\mathcal{Q}\|_{\tau p}}{\partial \mathcal{Q}} \times_3 F^H \right\|_F^2 \leq J_3 RC$$

is bounded. From the first-order optimality of (22), in $\mathcal{M}_{q < q >}$, we can deduce

$$\begin{aligned} \mathbf{0} &\in \beta_q \partial_{\mathcal{M}_{q < q >}^{k+1}} \|\mathcal{M}_{q < q >}^{k+1}\|_{\tau p} - \rho_q^k (\mathcal{B}^{k+1} - \mathcal{M}_q^{k+1} + \frac{\mathcal{T}_q^k}{\rho_q^k}) \\ &= \beta_q \partial_{\mathcal{M}_{q < q >}^{k+1}} \|\mathcal{M}_{q < q >}^{k+1}\|_{\tau p} - \mathcal{T}_q^{k+1}. \end{aligned}$$

Therefore, the sequence $\{\mathcal{T}_q^k\}_{q=1}^{N(N-1)/2}$ are bounded. \square

Theorem 5.1 (convergence analysis). The sequences $\{\mathcal{B}^k\}$ and $\{\mathcal{M}_q^k\}_{q=1}^{N(N-1)/2}$ generated by Algorithm 1 are Cauchy sequences and convergent.

Proof. First, regarding to \mathcal{B}^{k+1} , from (19), we have

$$\mathcal{T}_q^{k+1} = \mathcal{T}_q^k + \rho_q^k (\mathcal{B}^{k+1} - \mathcal{M}_q^{k+1}) \Rightarrow \mathcal{B}^{k+1} = \mathcal{M}_q^{k+1} + (\mathcal{T}_q^{k+1} - \mathcal{T}_q^k) / \rho_q^k.$$

To begin, we observe that $\mathcal{P}_\Omega(\mathcal{B}^{k+1}) = \mathcal{P}_\Omega(\mathcal{B}^k)$, which leads to the following deduction:

$$\begin{aligned} \|\mathcal{B}^{k+1} - \mathcal{B}^k\|_F &= \|\mathcal{P}_{\Omega^c}(\mathcal{B}^{k+1} - \mathcal{B}^k)\|_F \\ &= \left\| \mathcal{P}_{\Omega^c} \left(\mathcal{B}^{k+1} - \frac{\sum_q \rho_q^k}{\sum_q \rho_q^k} \mathcal{B}^k \right) \right\|_F \\ &= \left\| \mathcal{P}_{\Omega^c} \left(\mathcal{B}^{k+1} - \frac{\sum_q \rho_q^k (\mathcal{M}_q^k + (\mathcal{T}_q^k - \mathcal{T}_q^{k-1}) / \rho_q^{k-1})}{\sum_q \rho_q^k} \right) \right\|_F \\ &= \left\| \mathcal{P}_{\Omega^c} \left(\frac{\sum_q \rho_q^k ((\mathcal{M}_q^k - \mathcal{T}_q^k / \rho_q^k) - (\mathcal{M}_q^k + (\mathcal{T}_q^k - \mathcal{T}_q^{k-1}) / \rho_q^{k-1}))}{\sum_q \rho_q^k} \right) \right\|_F \\ &= \left\| \mathcal{P}_{\Omega^c} \left(\frac{\sum_q \rho_q^k (\mathcal{T}_q^k / \rho_q^k + (\mathcal{T}_q^k - \mathcal{T}_q^{k-1}) / \rho_q^{k-1})}{\sum_q \rho_q^k} \right) \right\|_F \\ &\leq \left\| \frac{\sum_q \rho_q^k (\mathcal{T}_q^k / \rho_q^k + (\mathcal{T}_q^k - \mathcal{T}_q^{k-1}) / \rho_q^{k-1})}{\sum_q \rho_q^k} \right\|_F \\ &\leq \sum_q \|(1 + \mu) \mathcal{T}_q^k / \rho_q^{k-1} - \mathcal{T}_q^{k-1} / \rho_q^{k-1}\|_F \end{aligned}$$

$$\leq \sum_q \frac{1}{\rho_q^0 \mu^{k-1}} (\|(1+\mu)\mathcal{T}_q^k\|_F + \|\mathcal{T}_q^{k-1}\|_F).$$

It is noted that $\{\mathcal{T}_q^k\}_{q=1}^{N(N-1)/2}$ are bounded, and since $\lim_{k \rightarrow \infty} \frac{1}{\mu^k} = 0$, we conclude that $\lim_{k \rightarrow \infty} \|\mathcal{B}^{k+1} - \mathcal{B}^k\|_F = 0$. For any $n < m$, applying the triangle inequality again yields:

$$\begin{aligned} \|\mathcal{B}^m - \mathcal{B}^n\|_F &\leq \sum_{k=n}^m \|\mathcal{B}^{k+1} - \mathcal{B}^k\|_F \\ &\leq \sum_{k=n}^m \sum_q \frac{1}{\rho_q^0 \mu^{k-1}} (\|(1+\mu)\mathcal{T}_q^k\|_F + \|\mathcal{T}_q^{k-1}\|_F) \\ &\leq \sum_{k=n}^m \frac{C_1}{\mu^{k-1}}, \end{aligned}$$

where C_1 is an upper bound for $\sum_q 1/\rho_q^0 (\|(1+\mu)\mathcal{T}_q^k\|_F + \|\mathcal{T}_q^{k-1}\|_F)$. Thus, we conclude that $\lim_{m,n \rightarrow \infty} \|\mathcal{B}^m - \mathcal{B}^n\|_F = 0$. Therefore, $\{\mathcal{B}^k\}$ is a Cauchy sequence, which is convergent.

Finally, for the sequence $\{\mathcal{M}_q^k\}_{q=1}^{N(N-1)/2}$, the following estimates can be derived:

$$\begin{aligned} \|\mathcal{M}_q^m - \mathcal{M}_q^n\|_F &\leq \sum_{k=n}^m \|\mathcal{M}_q^{k+1} - \mathcal{M}_q^k\|_F \\ &\leq \sum_{k=n}^m \|\mathcal{B}^{k+1} - (\mathcal{T}_q^{k+1} - \mathcal{T}_q^k)/\rho_q^k - \mathcal{B}^k + (\mathcal{T}_q^k - \mathcal{T}_q^{k-1})/\rho_{l_1 l_2}^{k-1}\|_F \\ &\leq \sum_{k=n}^m \|\mathcal{B}^{k+1} - \mathcal{B}^k\|_F + \frac{1}{\rho_q^k} \|\mathcal{T}_q^{k+1}\|_F + \frac{1+\mu}{\rho_q^k} \|\mathcal{T}_q^k\|_F + \frac{1}{\rho_q^{k-1}} \|\mathcal{T}_q^{k-1}\|_F \\ &\leq \sum_{k=n}^m \frac{C_1 + C_2}{\mu^{k-1}}, \end{aligned}$$

where C_2 is an upper bound for the following expression: $\frac{1}{\rho_q^0 \mu} \|\mathcal{T}_q^{k+1}\|_F + \frac{1+\mu}{\rho_q^0 \mu} \|\mathcal{T}_q^k\|_F + \frac{1}{\rho_q^0} \|\mathcal{T}_q^{k-1}\|_F$. Thus, we conclude that $\lim_{m,n \rightarrow \infty} \|\mathcal{M}_q^m - \mathcal{M}_q^n\|_F = 0$. Therefore, the sequence $\{\mathcal{M}_q^k\}_{q=1}^{N(N-1)/2}$ forms a Cauchy sequence, which implies its convergence. \square

Theorem 5.2 (Karush-Kuhn-Tucker conditions). Suppose that $\mathcal{N}^k = \{\mathcal{B}^k, \mathcal{M}_q^k, \mathcal{T}_q^k\}$ is generated from the proposed Algorithm 1, then the limit point $\mathcal{N}^* = \{\mathcal{B}^*, \mathcal{M}_q^*, \mathcal{T}_q^*\}$ is a stationary point, which is $\mathbf{0} \in \partial L(\mathcal{B}^*, \mathcal{M}_q^*, \mathcal{T}_q^*)$, or equivalently,

$$\mathcal{B}^* - \mathcal{M}_q^* = \mathbf{0}, \quad \mathcal{T}_{q < q}^* \in \partial_{\mathcal{M}_{q < q}} \|\mathcal{M}_{q < q}^*\|_{\tau p}, \quad \sum_q \mathcal{T}_q^* = \partial_{\mathcal{B}} \Phi(\mathcal{B}^*).$$

Proof. From Lemma 5.2, Theorem 5.1 and the Bolzano-Weierstrass theorem, there must be at least one accumulation point of the sequence $\{\mathcal{N}^k\}_{k=1}^{+\infty}$. We denote one of the points

$\mathcal{N}^* = \{\mathcal{B}^*, \mathcal{M}_q^*, \mathcal{T}_q^*\}$. Without loss of generality, we assume $\{\mathcal{N}^k\}_{k=1}^{+\infty}$ converge to \mathcal{N}^* . Since $(\mathcal{T}_q^{k+1} - \mathcal{T}_q^k)/\rho_q^k = \mathcal{B}^{k+1} - \mathcal{M}_q^{k+1}$, we have

$$\lim_{k \rightarrow \infty} (\mathcal{B}^{k+1} - \mathcal{M}_q^{k+1}) = \lim_{k \rightarrow \infty} (\mathcal{T}_q^{k+1} - \mathcal{T}_q^k)/\rho_q^k = \mathbf{0}.$$

Then $\mathcal{B}^* - \mathcal{M}_q^* = \mathbf{0}$ is obtained. From (22), we can deduce

$$\mathbf{0} \in \beta_q \partial_{\mathcal{M}_{q < q >}} \|\mathcal{M}_{q < q >}^{k+1}\|_{\tau p} + \rho_q^k (\mathcal{M}_{q < q >}^{k+1} - \mathcal{B}_{q < q >}^{k+1}) + \mathcal{T}_{q < q >}^k.$$

Then it follows that $\mathcal{T}_{q < q >}^* \in \partial_{\mathcal{M}_{q < q >}} \|\mathcal{M}_{q < q >}^*\|_{\tau p}$.

Similarly, from (20), we have

$$\begin{aligned} \mathbf{0} &= \sum_q \mathcal{T}_q^k + \rho_q^k (\mathcal{B}^{k+1} - \mathcal{M}_q^k) + \partial_{\mathcal{B}} \Phi(\mathcal{B}^{k+1}), \\ \lim_{k \rightarrow \infty} (\mathcal{T}_q^k + \rho_q^k (\mathcal{B}^{k+1} - \mathcal{M}_q^k)) &= (\mathcal{T}_q^* + \rho_q^* (\mathcal{B}^* - \mathcal{M}_q^*)) = \mathcal{T}_q^*. \end{aligned}$$

Then $\sum_q \mathcal{T}_q^* = \partial_{\mathcal{B}} \Phi(\mathcal{B}^*)$, where

$$\begin{cases} \partial_{\mathcal{B}} \Phi(\mathcal{B}^*)_{j_1, j_2, \dots, j_N} = 0, & \mathcal{P}_{\Omega}(\mathcal{B}_{j_1, j_2, \dots, j_N}) \neq \mathcal{P}_{\Omega}(\mathcal{O}_{j_1, j_2, \dots, j_N}), \\ \partial_{\mathcal{B}} \Phi(\mathcal{B}^*)_{j_1, j_2, \dots, j_N} = 1, & \mathcal{P}_{\Omega}(\mathcal{B}_{j_1, j_2, \dots, j_N}) = \mathcal{P}_{\Omega}(\mathcal{O}_{j_1, j_2, \dots, j_N}). \end{cases}$$

Therefore $\{\mathcal{B}^*, \mathcal{M}_q^*, \mathcal{T}_q^*\}$ satisfies the the Karush-Kuhn-Tucker conditions of the Lagrange function $L(\mathcal{B}, \mathcal{M}_q, \mathcal{T}_q)$. \square

6 Experiments

The performance of the proposed MPCP method is evaluated using several quality metrics, including peak signal-to-noise rate (PSNR) value, structural similarity (SSIM) value [28], feature similarity (FSIM) value [37], and the erreur relative globale adimensionnelle de synthèse (ERGAS) value [27]. Among these metrics, higher PSNR, SSIM, and FSIM values indicate better performance, while a lower ERGAS value is preferred. All experiments were conducted on a Windows 11 platform, using MATLAB (R2023b), with an 13th Gen Intel Core i5-13600K 3.50 GHz processor and 32 GB of RAM. Let J^c and J^r represent the complete and reference images, respectively, while J_1 and J_2 denote the spatial dimensions of the image.

1. PSNR is defined as: $\text{PSNR} := 10 \log_{10}(\frac{255^2 \times J_1 J_2}{\|J^r - J^c\|_2^2})$.

2. SSIM is defined as: $\text{SSIM} := \frac{(2\mu_{J^c} \mu_{J^r} + c_1)(2\sigma_{J^c J^r} + c_2)}{(\mu_{J^c}^2 + \mu_{J^r}^2 + c_1)(\sigma_{J^c}^2 + \sigma_{J^r}^2 + c_2)}$, where μ_{J^c} is average of J^c ; σ_{J^c} is the variance of J^c , and $\sigma_{J^c J^r}$ is the covariance of J^c and J^r .

3. FSIM is defined as: $\text{FSIM} := \frac{\sum_{x \in \Omega} S_L(x) \cdot PC_m(x)}{\sum_{x \in \Omega} PC_m(x)}$, where $S_L(x)$ is derived from the

phase congruency and the image gradient magnitude of J^c and J^r ; $PC_m(x)$ is the maximum phase congruency of PC_c (for J^c) and PC_r (for J^r); and Ω represents the entire airspace of the image.

When calculating the PSNR, SSIM, and FSIM values for the tensor image, each slice of the tensor is computed first, and then the average value is taken across slices.

4. ERGAS for $\mathcal{A}, \mathcal{B} \in \mathbb{R}^{J_1 \times J_2 \times J_3}$ is defined as:

$$\text{ERGAS} := 100 \sqrt{\frac{\sum_{j=1}^{J_3} (\text{mse}(\mathcal{A}(:, :, j) - \mathcal{B}(:, :, j)) / (\text{mean2}(\mathcal{A}(:, :, j))))}{J_3}},$$

where `mse` is mean squared error performance function, and `mean2` is average of matrix elements.

5. For a tensor $\mathcal{B} \in \mathbb{R}^{J_1 \times J_2 \times \dots \times J_N}$, its sampling rate (SR) is defined as $\frac{\text{num}(\Omega)}{\prod_{j=1}^N J_j} \times 100\%$, where Ω denotes an index set of observed data; `num`(Ω) is the total number of elements in index set Ω .

6.1 Low-rank tensor completion

In this section, four sets of tensor data are tested: magnetic resonance imaging (MRI), multispectral image (MSI), color video (CV), and Light Field Images (LFI). Among them, MRI and MSI are third-order tensors, CV is a fourth-order tensor, and LFI is a fifth-order tensor. The data sampling method used is purely random sampling. The following LRTC methods are compared: HaLRTC [18] and TMCP [2], which represent the state-of-the-art approach based on Tucker decomposition. And the t-SVD-based methods: TNN [34], PSTNN [8], DCTTNN [19], TTNN [21], FTNN [9], WSTNN [39], t- ϵ -LogDet [31], and BEMCP [36]. Each method is tested using its respective optimal parameters. Since the t-SVD-based methods are applicable only to third-order tensors, for the tests involving fourth-order and fifth-order tensors, the data are reshaped into third-order tensors before applying these methods.

6.1.1 MRI completion

The performance of the proposed method, as well as the comparative methods, is evaluated on MRI¹ data with dimensions $181 \times 217 \times 181$. Initially, the visual quality of the MRI data recovered at sampling rates of 5%, 10% and 20% are demonstrated in Figs. 3-5. It is evident that the proposed method outperforms the comparative methods. As shown in Fig. 3, the image recovered using the proposed method at a 5% sampling rate exhibits successful overall reconstruction. With an increase in the sampling rate, further image details are progressively restored, as illustrated in Figs. 4 and 5.

Subsequently, the average quantitative results of the frontal slices of the MRI, restored by all methods at various sampling rates, are presented in Table 1. The optimal results are highlighted in bold. The proposed method demonstrates a 2.7 dB higher PSNR value compared to the suboptimal LPRN method at a 5% sampling rate, alongside significant improvements in SSIM, FSIM, and ERGAS values.

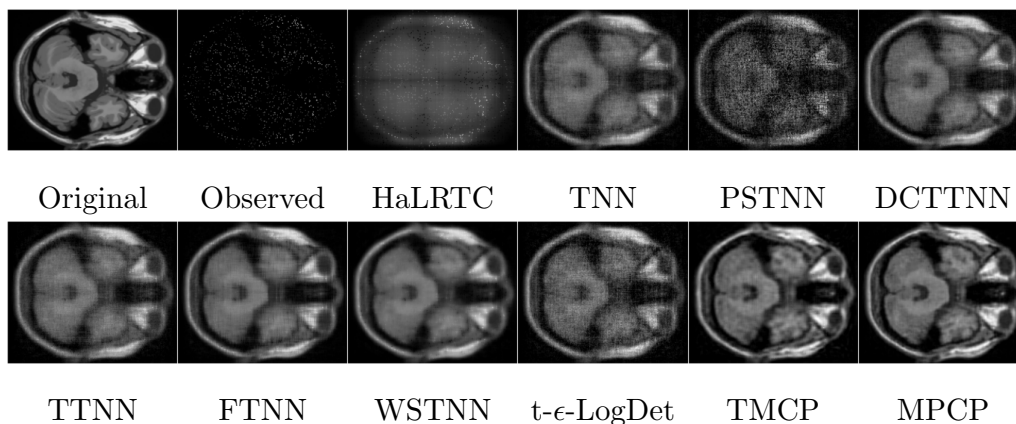


Figure 3: Visual results of the 40th slice of the MRI data at a sampling rate of 5%.

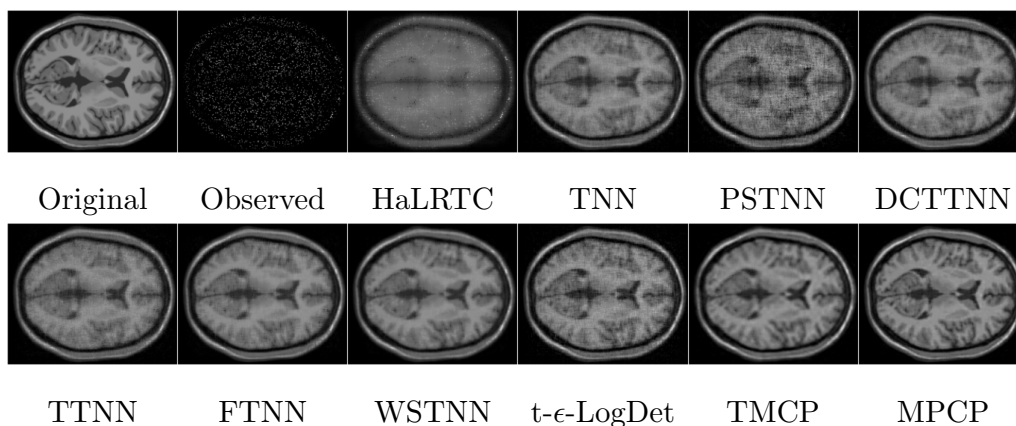


Figure 4: Visual results of the 80th slice of the MRI data at a sampling rate of 10%.

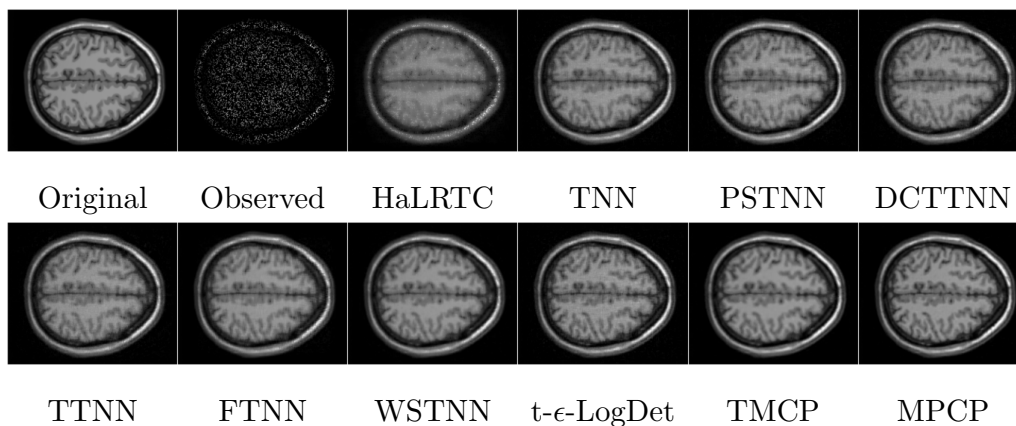


Figure 5: Visual results of the 120th slice of the MRI data at a sampling rate of 20%.

Table 1: The PSNR, SSIM, FSIM and ERGAS values for MRI tested by observed and the ten utilized LRTC methods.

SR	5%				10%				20%			
Method	PSNR	SSIM	FSIM	ERGAS	PSNR	SSIM	FSIM	ERGAS	PSNR	SSIM	FSIM	ERGAS
Observed	11.399	0.310	0.530	1021.079	11.635	0.323	0.565	993.760	12.148	0.350	0.612	936.741
HaLRTC	17.297	0.298	0.637	537.432	20.146	0.439	0.726	389.074	24.454	0.660	0.829	234.870
TNN	22.691	0.470	0.743	304.114	26.097	0.643	0.812	204.863	29.963	0.799	0.882	130.769
PSTNN	16.166	0.197	0.588	608.853	22.453	0.439	0.723	307.529	29.566	0.767	0.870	137.477
DCTTNN	23.280	0.507	0.755	277.284	26.066	0.655	0.815	198.957	30.167	0.818	0.888	122.854
TTNN	23.363	0.494	0.755	275.704	26.384	0.651	0.818	189.680	30.440	0.814	0.890	117.127
FTNN	24.575	0.688	0.832	240.235	27.658	0.806	0.885	164.653	31.833	0.908	0.938	99.941
WSTNN	25.519	0.708	0.824	212.073	29.036	0.836	0.887	139.526	33.441	0.929	0.940	83.149
t- ϵ -LogDet	21.161	0.340	0.677	357.989	26.670	0.613	0.798	192.217	31.480	0.811	0.888	109.610
TMCP	27.862	0.735	0.839	154.266	30.595	0.861	0.891	112.631	34.360	0.944	0.944	73.017
MPCP	30.573	0.855	0.895	115.228	33.700	0.920	0.932	80.246	37.339	0.962	0.963	52.177

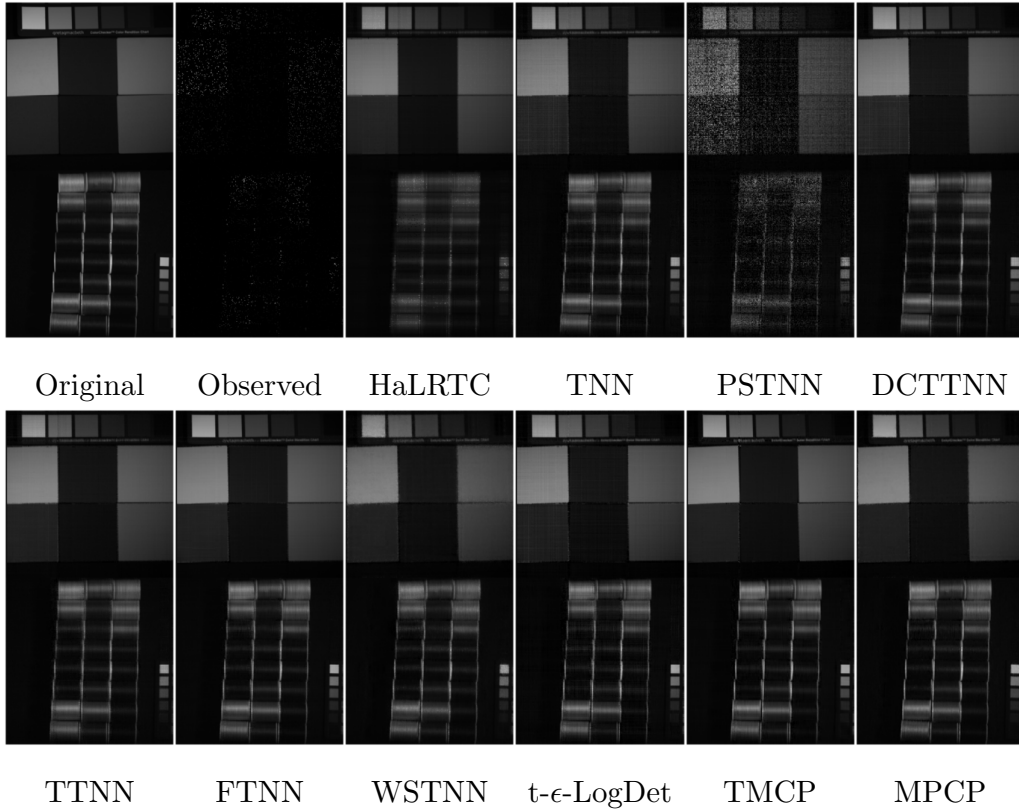


Figure 6: Visual results for MSI data. The rows of MSIs are in order: sponges, thread_spools. SR: 5%. The corresponding bands in each row are: 10, 5.

6.1.2 MSI completion

The test dataset used in this experiment consists of six MSIs: chart_and_stuffed_toy, thread_spools, fake_and_real_lemons, fake_and_real_tomatoes, real_and_fake_peppers, and sponges. All testing data have dimensions of $256 \times 256 \times 31$, where the spatial resolution

¹http://brainweb.bic.mni.mcgill.ca/brainweb/selection_normal.html

is 256×256 and the spectral resolution is 31. Visual results for different sampling rates and bands are presented in Figs. 6-8. The specific MSI names and their corresponding bands are provided in the figure captions.

As shown in Figs. 6-8, the visual quality of the results obtained using the MPCP method surpasses that of the comparative methods at all three sampling rates. In particular, Fig. 6 demonstrates that the MPCP method is more effective in tensor recovery when compared to the suboptimal methods. For example, the image recovered using the MPCP method reveals the sponges more clearly, while the image recovered using the suboptimal FTNN method still contains significant noise and artifacts.

To further emphasize the superiority of the proposed method, the average quantitative results for the six MSIs are summarized in Table 2. The proposed method demonstrates a significant improvement, achieving at least 4.2 dB higher PSNR for image recovery compared to the suboptimal WSTNN method at both 10% and 20% sampling rates. Moreover, at the same sampling rates, the SSIM, FSIM, and ERGAS values obtained by the proposed method are markedly superior to those of the WSTNN method. At a 5% sampling rate, where the suboptimal method is the TMCP method, the proposed method still outperforms TMCP method by 3.5 dB in terms of PSNR and also achieves a substantially higher SSIM value.

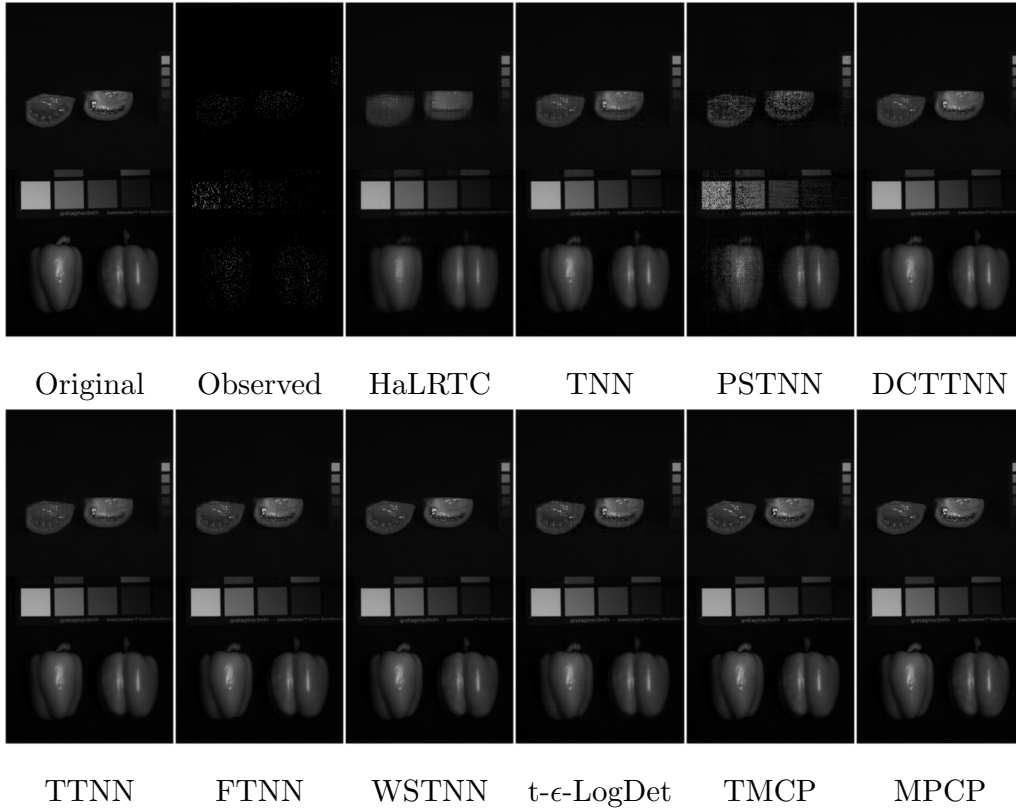


Figure 7: Visual results for MSI data. The rows of MSIs are in order: fake_and_real.tomatoes, real_and_fake.peppers. SR: 10%. The corresponding bands in each row are: 20, 15.

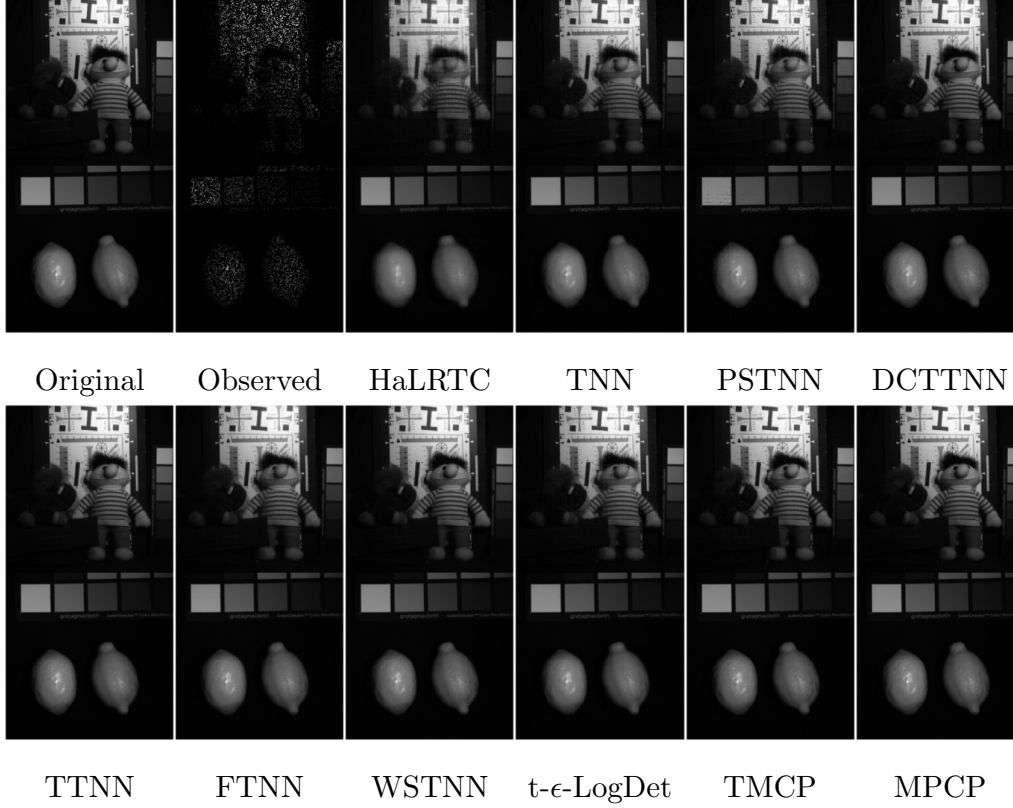


Figure 8: Visual results for MSI data. The rows of MSIs are in order: chart_and_stuffed_toy, fake_and_real_lemons. SR: 20%. The corresponding bands in each row are: 30, 25.

Table 2: The average PSNR, SSIM, FSIM and ERGAS values for six MSIs tested by observed and the ten utilized LRTC methods.

SR	5%				10%				20%			
Method	PSNR	SSIM	FSIM	ERGAS	PSNR	SSIM	FSIM	ERGAS	PSNR	SSIM	FSIM	ERGAS
Observed	14.956	0.167	0.675	891.700	15.190	0.210	0.665	867.956	15.703	0.287	0.654	818.238
HaLRTC	28.138	0.867	0.893	212.430	33.040	0.931	0.939	123.174	38.396	0.971	0.972	68.326
TNN	32.694	0.897	0.915	127.707	37.576	0.954	0.958	75.302	43.342	0.983	0.984	40.452
PSTNN	18.744	0.541	0.660	565.723	24.036	0.737	0.804	314.595	39.247	0.967	0.968	67.796
DCTTNN	35.034	0.935	0.942	95.770	39.971	0.973	0.974	56.226	45.945	0.991	0.991	29.589
TTNN	34.907	0.940	0.946	97.114	40.447	0.979	0.980	51.580	47.066	0.994	0.994	24.567
FTNN	36.514	0.956	0.958	81.911	41.244	0.981	0.980	48.205	46.930	0.993	0.993	26.680
WSTNN	33.452	0.822	0.929	166.546	42.221	0.988	0.987	38.839	49.899	0.997	0.997	16.421
t- ϵ -LogDet	33.826	0.890	0.909	113.213	39.689	0.963	0.964	59.623	45.345	0.987	0.987	33.042
TMCP	37.126	0.949	0.950	73.914	42.180	0.978	0.976	42.218	47.418	0.991	0.991	23.654
MPCP	40.676	0.981	0.978	46.355	46.646	0.995	0.994	23.322	54.117	0.999	0.999	10.135

6.1.3 CV completion

We conduct tests on three CVs², namely akiyo, coastguard, and hall, each with dimensions $144 \times 176 \times 3 \times 50$, where the number of frames is 50 and each frame is a color image of size $144 \times 176 \times 3$. The visual results for these three CVs are presented in Figs. 9-11.

²<http://trace.eas.asu.edu/yuv/>

The number of frames and corresponding sampling rates for each CV are specified in the figure captions.

As shown in Figs. 9-11, the proposed method consistently produces superior visual recovery compared to the other methods. In particular, Fig. 9 illustrates that the proposed method effectively restores detailed features of the person in the image, such as facial characteristics, while the comparison methods still exhibit considerable blurriness in recovering these details.

To further substantiate the superiority of the proposed method, the average quantitative results for the three CVs are summarized in Table 3. Evaluating metrics such as PSNR, SSIM, FSIM, and ERGAS values, the proposed method outperforms the other methods at various sampling rates. Notably, it achieves a PSNR value that is at least 2.3 dB higher than the suboptimal WSTNN method.

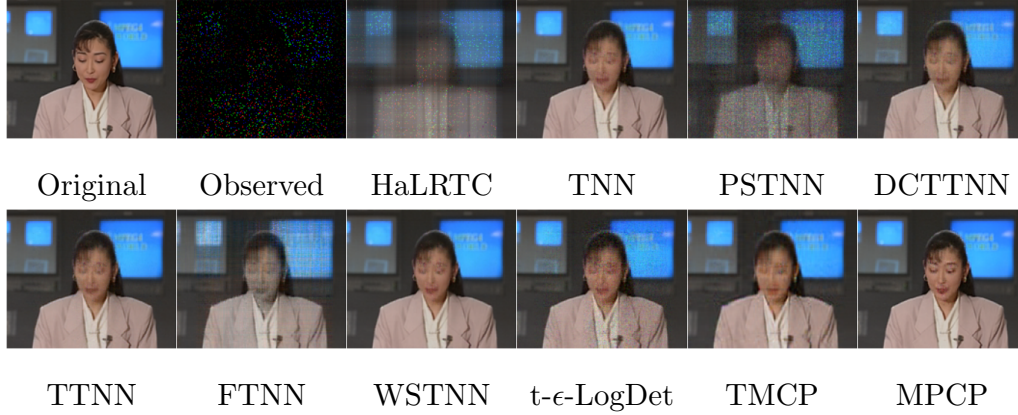


Figure 9: Visual results of the 15th frame of the akiyo data at a sampling rate of 5%.

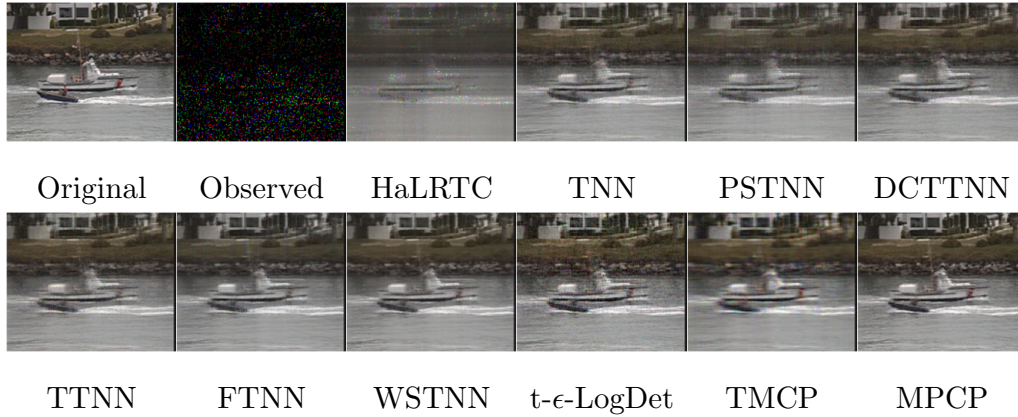


Figure 10: Visual results of the 30th frame of the coastguard data at a sampling rate of 10%.

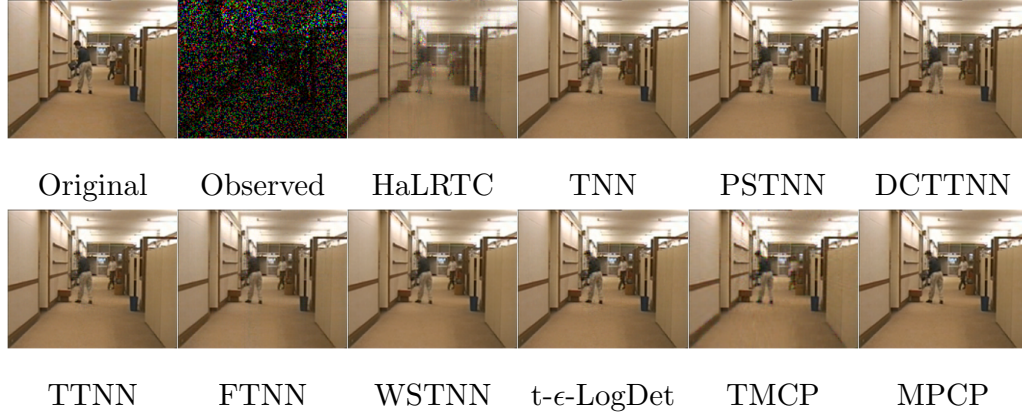


Figure 11: Visual results of the 45th frame of the hall data at a sampling rate of 20%.

Table 3: The average PSNR, SSIM, FSIM and ERGAS values for three CVs tested by observed and the ten utilized LRTC methods.

SR	5%				10%				20%			
Method	PSNR	SSIM	FSIM	ERGAS	PSNR	SSIM	FSIM	ERGAS	PSNR	SSIM	FSIM	ERGAS
Observed	6.554	0.012	0.417	1144.119	6.789	0.021	0.433	1113.472	7.301	0.038	0.456	1049.787
HaLRTC	17.036	0.463	0.685	345.162	20.935	0.611	0.769	221.104	25.049	0.773	0.862	141.290
TNN	27.879	0.791	0.898	111.919	30.760	0.855	0.931	84.050	33.835	0.907	0.955	61.992
PSTNN	15.637	0.326	0.696	403.452	27.398	0.796	0.896	113.445	33.383	0.906	0.953	64.321
DCTTNN	27.375	0.774	0.893	117.217	29.970	0.842	0.924	89.617	33.334	0.904	0.954	63.695
TTNN	28.413	0.805	0.904	106.046	31.235	0.866	0.935	80.345	34.775	0.923	0.962	55.778
FTNN	25.037	0.756	0.866	148.398	28.449	0.852	0.915	99.763	32.132	0.922	0.953	66.211
WSTNN	29.485	0.864	0.917	92.928	32.722	0.917	0.949	67.230	36.500	0.958	0.973	45.013
t- ϵ -LogDet	20.854	0.494	0.783	244.032	31.539	0.846	0.935	81.087	34.895	0.905	0.959	57.988
TMCP	27.286	0.788	0.879	112.108	28.845	0.833	0.903	94.287	31.138	0.892	0.935	73.240
MPCP	31.786	0.888	0.944	75.478	35.278	0.936	0.966	52.651	39.432	0.970	0.984	33.166

6.1.4 LFI completion

In this section, the proposed method is evaluated using the Antinous dataset from the HCI 4D LFI³. The size of the Antinous data is $128 \times 128 \times 3 \times 9 \times 9$, making it a fifth-order tensor. This dataset consists of 81 different views arranged in a 9×9 grid. To quantitatively assess the performance of the completion method, we computed the average quantitative results for the 81 color images, each with dimensions $128 \times 128 \times 3$. The average quantitative results for the Antinous dataset are presented in Table 4.

Considering metrics such as PSNR, SSIM, FSIM, and ERGAS, the proposed method outperforms all other methods across various sampling rates. The suboptimal method in this comparison is the WSTNN method. Specifically, the proposed method achieves a PSNR value that is at least 4.0 dB higher than that of the suboptimal WSTNN method.

Additionally, the visual results at 5% - 20% sampling rates are shown in Figs. 12-14. As illustrated, the proposed method yields the best visual recovery. Notably, the reconstruction of the statue's head is significantly clearer and more detailed compared to the other methods.

³<https://lightfield-analysis.uni-konstanz.de/>

Table 4: The average PSNR, SSIM, FSIM and ERGAS values for LFI tested by observed and the ten utilized LRTC methods.

SR	5%				10%				20%			
Method	PSNR	SSIM	FSIM	ERGAS	PSNR	SSIM	FSIM	ERGAS	PSNR	SSIM	FSIM	ERGAS
Observed	8.107	0.014	0.510	1035.474	8.341	0.021	0.462	1007.901	8.853	0.030	0.402	950.167
HaLRTC	17.753	0.593	0.778	341.075	22.228	0.707	0.839	203.733	28.175	0.861	0.917	102.896
TNN	31.916	0.912	0.949	69.625	34.771	0.947	0.969	51.419	38.661	0.973	0.984	33.961
PSTNN	18.718	0.467	0.743	307.351	31.556	0.910	0.948	71.712	37.947	0.970	0.982	36.886
DCTTNN	31.760	0.907	0.949	70.430	34.041	0.939	0.966	55.074	37.592	0.968	0.982	37.638
TTNN	32.758	0.929	0.959	62.807	36.189	0.963	0.979	43.003	40.609	0.984	0.991	26.179
FTNN	28.609	0.847	0.915	98.810	31.028	0.903	0.946	75.189	34.058	0.945	0.968	53.542
WSTNN	33.617	0.950	0.963	58.507	37.481	0.975	0.981	38.595	42.447	0.989	0.993	22.472
t- ϵ -LogDet	24.161	0.720	0.865	163.363	36.073	0.952	0.972	44.400	40.512	0.979	0.987	27.869
TMCP	31.909	0.912	0.940	67.109	33.974	0.937	0.956	52.922	36.086	0.959	0.971	41.543
MPCP	37.658	0.971	0.981	39.040	42.075	0.986	0.991	23.979	46.931	0.994	0.996	13.903

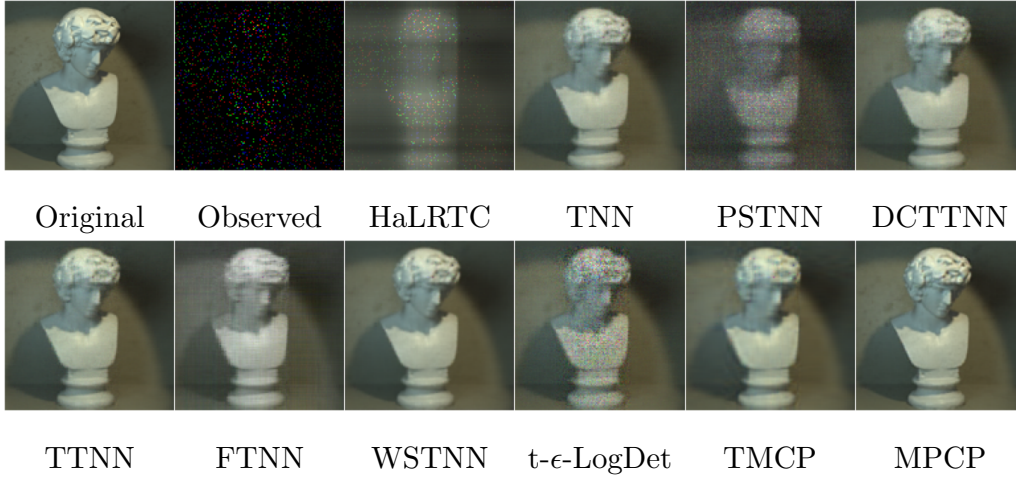


Figure 12: Visual results of LFI data at a sampling rate of 5%. The image located at the (3, 3)-th grid of Antinous

6.2 Discussion

6.2.1 Parameters setting

The proposed method utilizes the N-tubal rank framework, which allows for the selection of the parameters β and ρ based on the parameter settings from [39]. In this section, we analyze the impact of different parameters on the tensor p -th order τ norm. All tests are conducted using the MSI dataset “chart_and_stuffed_toy”.

Given that the choice of parameter τ depends on the value of p , the performance of the proposed method is evaluated at a 5% sampling rate under various settings of p and τ^p . The parameter p is selected from the set $\{0.1 : 0.1 : 0.9\}$, and τ^p is chosen from the set $\{50, 100, 150, 200\}$. The PSNR values corresponding to different conditions are presented in Table 5.

As shown in the table, recovery performance improves significantly as the value of p decreases. Specifically, when $p = 0.1$, the PSNR value increases by 0.75 dB compared to

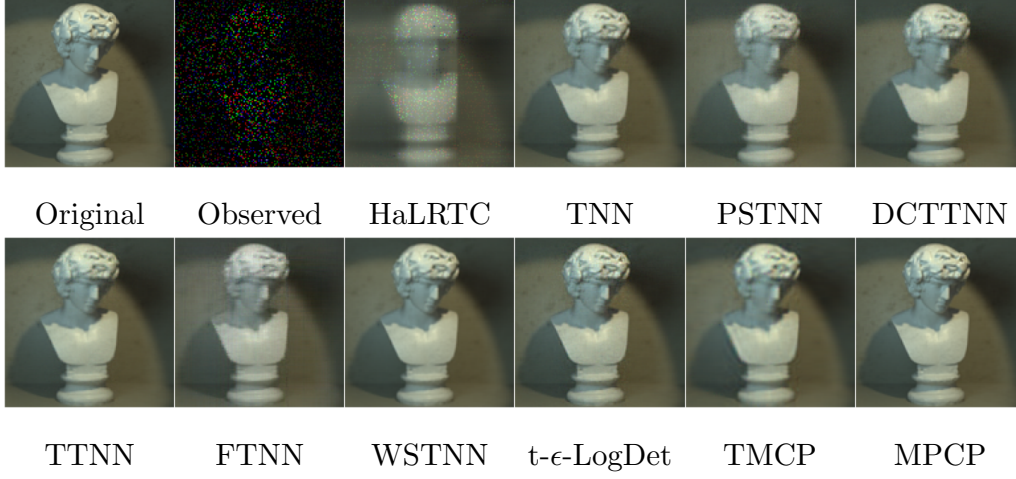


Figure 13: Visual results for MRI data. MR: top row is 95%, and last row is 90%. The corresponding slices in each row are: 50, 100.

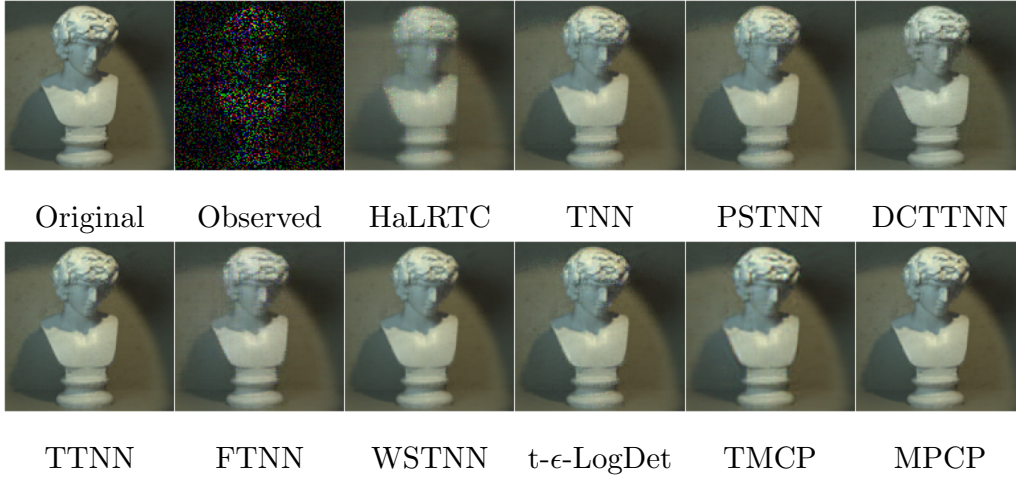


Figure 14: Visual results for MRI data. MR: top row is 95%, and last row is 90%. The corresponding slices in each row are: 50, 100.

Table 5: The PSNR value with different τ^p and p of tensor p -th order τ norm.

$\tau^p \backslash p$	0.9	0.8	0.7	0.6	0.5	0.4	0.3	0.2	0.1
50	16.899	16.901	16.903	16.907	16.911	16.914	16.918	16.924	16.942
100	34.734	34.824	34.923	35.031	35.143	35.258	35.362	35.441	35.484
150	34.371	34.473	34.590	34.724	34.869	35.037	35.204	35.359	35.508
200	34.086	34.202	34.332	34.479	34.639	34.812	34.993	35.171	35.338

when $p = 0.9$. This finding supports our theoretical analysis: for the same τ^p , the penalty applied to smaller singular values increases as p decreases. Based on this observation, the value of p is selected to be 0.1. Additionally, Table 6 lists the optimal τ^p values for

different images across various sampling rates.

Table 6: The optimal τ^p values for different images at various sampling rates.

Image \ SR	SR			Image \ SR	SR		
	5%	10%	20%		5%	10%	20%
chart_and_stuffed_toy	120	70	40	MRI	80	50	30
fake_and_real_lemons	50	30	20	akiyo	120	50	50
fake_and_real_tomatoes	50	30	20	coastguard	330	180	90
real_and_fake_peppers	60	40	30	hall	290	100	60
sponges	110	80	60	antinous	140	90	80
thread_spools	70	40	30				

6.2.2 Ablation study

In this section, the advantages of the MPCP function over the traditional MCP function are further validated. A comparison is made with a variant model that uses the MCP function (referred to as the MCP method). Quantitative results for various images and sampling rates are presented in Table 7. The results demonstrate that the MPCP method outperforms the MCP method. Moreover, at higher sampling rates, the performance gap between the MPCP and MCP methods continues to expand, further supporting our theoretical analysis. Specifically, the MPCP function not only protects larger singular values more effectively but also penalizes smaller singular values more efficiently, thereby addressing the MCP function’s limitation in penalizing small singular values.

Table 7: The quantitative results at different images and sampling rates

	Image	chart_and_stuffed_toy		MRI		akiyo		antinous	
SR	Method	MCP	MPCP	MCP	MPCP	MCP	MPCP	MCP	MPCP
5%	PSNR	34.555	35.553	29.112	30.573	36.041	36.849	35.545	37.658
	SSIM	0.950	0.960	0.823	0.855	0.974	0.977	0.962	0.971
	FSIM	0.958	0.964	0.875	0.895	0.983	0.986	0.973	0.981
	ERGAS	75.911	67.630	137.366	115.228	41.464	38.048	48.398	39.040
10%	PSNR	40.445	42.215	32.058	33.700	40.228	41.689	40.279	42.075
	SSIM	0.984	0.989	0.898	0.920	0.989	0.991	0.983	0.986
	FSIM	0.987	0.990	0.917	0.932	0.992	0.994	0.988	0.991
	ERGAS	38.898	31.639	97.716	80.246	26.498	22.814	28.874	23.979
20%	PSNR	48.004	50.796	35.561	37.339	44.601	46.596	44.989	46.931
	SSIM	0.996	0.998	0.950	0.962	0.995	0.996	0.992	0.994
	FSIM	0.997	0.998	0.953	0.963	0.997	0.998	0.995	0.996
	ERGAS	17.120	12.361	64.788	52.177	16.582	13.501	17.153	13.903

7 Conclusion

This paper proposes a novel non-convex function, the MPCP function. The MPCP function not only effectively protects large singular values but also imposes a strong penalty on small singular values, addressing a key limitation of the MCP function in penalizing smaller singular values. Both theoretical analysis and experimental results demonstrate the superiority of the MPCP function over the MCP function. As a non-convex relaxation for the LRTC problem, the tensor p -th order τ norm is derived. We then investigate the LRTC model based on the MPCP function and its corresponding solution algorithm. Extensive experiments reveal that the proposed method outperforms the comparison methods in both visual and numerical quantitative results. In the future, we aim to explore the application of the proposed function in tensor robust principal component analysis (TRPCA), specifically examining how its properties may change depending on the problem at hand. Additionally, given the use of the l_1 norm in TRPCA, we intend to investigate whether the proposed function can serve as a non-convex relaxation and analyze its associated properties.

Acknowledgments

This work was supported by the National Nature Science Foundation of China under Grant 12471353.

References

- [1] Boyd S, Parikh N, Chu E, 2011 Distributed optimization and statistical learning via the alternating direction method of multipliers *Found. Trends Mach. Learn.* **3(1)** 1-122
- [2] Chen P, Li F, Wei D, Lu C, 2024 Spatiotemporal traffic data completion with truncated minimax-concave penalty *Transp. Res. Part C Emerging Technol.* **164** 104657
- [3] Gu S, Zhang L, Zuo W, Feng X, 2014 Weighted nuclear norm minimization with application to image denoising *in: Proceedings of the IEEE Conference on Computer Vision and Pattern Recognition* pp 2862-2869
- [4] Gong P, Zhang C, Lu Z, Huang J, and Ye J, 2013 A general iterative shrinkage and thresholding algorithm for non-convex regularized optimization problems *Proceedings of the 30th International Conference on Machine Learning, PMLR* **28(2)** 37-45
- [5] Harshman R A, 1970 Foundations of the PARAFAC procedure: models and conditions for an “explanatory” multimodal factor analysis *UCLA Work. Paper. Phonetic.* **16(1)** 84
- [6] Hillar C J, Lim L, 2013 Most tensor problems are NP-hard *J. ACM* **60(6)** 1-39
- [7] Jiang W, Zhang J, Zhang C, Wang L, and Qi H, 2023 Robust low tubal rank tensor completion via factor tensor norm minimization *Pattern Recognit.* **135** 109169

- [8] Jiang T, Huang T, Zhao X, Deng L, 2020 Multi-dimensional imaging data recovery via minimizing the partial sum of tubal nuclear norm *J. Comput. Appl. Math.* **372** 112680
- [9] Jiang T, Ng M K, Zhao X, Huang T, 2020 Framelet representation of tensor nuclear norm for third-order tensor completion *IEEE Trans. Image Process.* **29** 7233-7244
- [10] Kong W, Zhang F, Qin W, Wang J, 2023 Low-tubal-rank tensor recovery with multilayer subspace prior learning *Pattern Recognit.* **140** 109545
- [11] Kilmer M E, Braman K, Hao N, Hoover R C, 2013 Third-order tensors as operators on matrices: A theoretical and computational framework with applications in imaging *SIAM J. Matrix Anal. Appl.*, **34**(1) 148-172
- [12] Kilmer M E, Martin C D, 2011 Factorization strategies for third-order tensors *Linear Algebra Appl.* **435**(3) 641-658
- [13] Kong H, Xie X, and Lin Z, 2018 t-schatten- p norm for low-rank tensor recovery *IEEE J. Sel. Top. Signal Process.* **12**(6) 1405-1419
- [14] Kolda T G, Bader B W, 2009 Tensor decompositions and applications *SIAM Rev.* **51**(3) 455-500
- [15] Liao T, Wu Z, Chen C, Zheng Z, Zhang X, 2023 Tensor completion via convolutional sparse coding with small samples-based training *Pattern Recognit.* **141** 109624
- [16] Lu C, Feng J, Chen Y, Liu W, Lin Z, Yan S, 2020 Tensor robust principal component analysis with a new tensor nuclear norm *IEEE Trans. Pattern Anal. Mach. Intell.* **42**(4) 925-938
- [17] Lewis A S, Sendov H S, 2005 Nonsmooth analysis of singular values *Part I: Theory, Set-Valued Analysis* **13**(3) 213-241
- [18] Liu J, Musialski P, Wonka P, Ye J, 2013 Tensor completion for estimating missing values in visual data *IEEE Trans. Pattern Anal. Mach. Intell.* **35**(1) 208-220
- [19] Lu C, Peng X, Wei Y, 2019 Low-rank tensor completion with a new tensor nuclear norm induced by invertible linear transforms *in: Proceedings of the IEEE Conference on Computer Vision and Pattern Recognition* pp 5996-6004
- [20] Mirsky L, 1975 A trace inequality of John von Neumann *Monatsh. Math.* **79**(4) 303-306
- [21] Ng M K, Zhang X, Zhao X, 2020 Patched-tube unitary transform for robust tensor completion *Pattern Recognit.* **100** 107181
- [22] Pokala P K, Hemadri R V, Seelamantula C S, 2022 Iteratively reweighted minimax-concave penalty minimization for accurate low-rank plus sparse matrix decomposition *IEEE Trans. Pattern Anal. Mach. Intell.* **44**(12) 8992-9010
- [23] Qiu D, Bai M, Ng M K, Zhang X, 2021 Nonlocal robust tensor recovery with non-convex regularization *Inverse Probl.* **37**(3) 035001

- [24] Rotfel'd S Yu, 1969 The singular numbers of the sum of completely continuous operators *in Spectral Theory, Boston, MA:Springer* pp 73–78
- [25] Tucker L R, 1966 Some mathematical notes on three-mode factor analysis *Psychometrika* **31(3)** 279–311
- [26] Wu J, Yin S, Jiang T, Liu G, Zhao X, 2025 PALADIN: a novel plug-and-play 3D CS-MRI reconstruction method *Inverse Probl.* **41(3)** 035014
- [27] Wald L, 2002 Data fusion: definitions and architectures: fusion of images of different spatial resolutions *Paris, France: Presses de l'Ecole, Ecole des Mines de Paris*
- [28] Wang Z, Bovik A, Sheikh H, Simoncelli E, 2004 Image quality assessment: from error visibility to structural similarity *IEEE Trans. Image Process.* **13(4)** 600-612
- [29] Xue J, Zhao Y, Liao W, Chan J Cheung-Wai, 2019 Nonconvex tensor rank minimization and its applications to tensor recovery *Inf. Sci.* **503** 109-128
- [30] You J, Jiao Y, Lu X, and Zeng T, 2019 A nonconvex model with minimax concave penalty for image restoration *J. Sci. Comput.* **78(2)** 1063-1086
- [31] Yang M, Luo Q, Li W, Xiao M, 2022 3-D array image data completion by tensor decomposition and nonconvex regularization approach *IEEE Trans. Signal Process.* **70** 4291–4304
- [32] Yang M, Luo Q, Li W, Xiao M, Nonconvex 3d array image data recovery and pattern recognition under tensor framework *Pattern Recognit.* **122** 108311
- [33] Zhang Z, Ely G, Aeron S, Hao N, Kilmer M, 2014 Novel methods for multilinear data completion and De-noising based on tensor-SVD *in: Proceedings of the IEEE Conference on Computer Vision and Pattern Recognition* pp 3842-3849
- [34] Zhang Z, Aeron S, 2017 Exact tensor completion using t-SVD *IEEE Trans. Signal Process.* **65(6)** 1511-1526
- [35] Zhang H, Fan H, Li Y, Liu X, Liu C, Zhu X, 2023 Tensor recovery based on a novel non-convex function minimax logarithmic concave penalty function *IEEE Trans. Image Process.* **32** 3413–3428
- [36] Zhang H, Fan H, Li Y, 2024 Tensor recovery based on bivariate equivalent minimax-concave penalty *Pattern Recognit.* **149** 110253
- [37] Zhang L, Zhang L, Mou X, Zhang D, 2011 FSIM: A feature similarity index for image quality assessment *IEEE Trans. Image Process.* **20(8)** 2378-2386
- [38] Zhang C, 2010 Nearly unbiased variable selection under minimax concave penalty *The Annals of statistics* **38(2)** 894-942
- [39] Zheng Y, Huang T, Zhao X, Jiang T, Ji T, Ma T, 2020 Tensor N-tubal rank and its convex relaxation for low-rank tensor recovery *Inf. Sci.* **532** 170–189